And yet it flips: connecting galactic spin and the cosmic web

Katarina Kraljic, Romeel Dave, Christophe Pichon

Monthly Notices
of the
ROYAL ASTRONOMICAL SOCIETY

MNRAS **493,** 362–381 (2020)
Advance Access publication 2020 January 28

doi:10.1093/mnras/staa250

And yet it flips: connecting galactic spin and the cosmic web

Katarina Kraljic,[1]★ Romeel Davé[1,2,3] and Christophe Pichon[4,5]

[1]*Institute for Astronomy, Royal Observatory, Edinburgh EH9 3HJ, UK*
[2]*University of the Western Cape, Bellville, Cape Town 7535, South Africa*
[3]*South African Astronomical Observatories, Observatory, Cape Town 7925, South Africa*
[4]*UMR 7095, Institut d'Astrophysique de Paris, Sorbonne Universités, UPMC Univ Paris 6 et CNRS, 98 bis Boulevard Arago, 75014 Paris, France*
[5]*Korea Institute for Advanced Study (KIAS), 85 Hoegiro, Dongdaemun-gu, Seoul 02455, Republic of Korea*

Accepted 2020 January 22. Received 2020 January 22; in original form 2019 June 3

ABSTRACT

We study the spin alignment of galaxies and haloes with respect to filaments and walls of the cosmic web, identified with DisPerSE , using the Simba simulation from $z = 0 - 2$. Massive haloes' spins are oriented perpendicularly to their closest filament's axis and walls, while low-mass haloes tend to have their spins parallel to filaments and in the plane of walls. A similar mass-dependent spin flip is found for galaxies, albeit with a weaker signal particularly at low mass and low-z, suggesting that galaxies' spins retain memory of their larger scale environment. Low-z star-forming and rotation-dominated galaxies tend to have spins parallel to nearby filaments, while quiescent and dispersion-dominated galaxies show preferentially perpendicular orientation; the star formation trend can be fully explained by the stellar mass correlation, but the morphology trend cannot. There is a dependence on HI mass, such that high-HI galaxies tend to have parallel spins while low-HI galaxies are perpendicular, suggesting that HI content may trace anisotropic infall more faithfully than the stellar component. Finally, at fixed stellar mass, the strength of spin alignments correlates with the filament's density, with parallel alignment for galaxies in high density environments. These findings are consistent with conditional tidal torque theory, and highlight a significant correlation between galactic spin and the larger scale tides that are important e.g., for interpreting weak lensing studies. Simba allows us to rule out numerical grid locking as the cause of previously-seen low mass alignment.

Key words: hydrodynamics – galaxies: evolution – galaxies: formation – galaxies: kinematics and dynamics – large-scale structure of universe.

1 INTRODUCTION

Understanding the origin of the diversity of galaxy morphologies seen today, the so-called Hubble sequence, is one of the biggest challenges for the theory of galaxy formation. The morphology of galaxies is intimately related to their angular momentum, which is acquired from the large-scale structure of the Universe through cosmic flows of matter, mergers, and interactions. The theory of structure formation thus suggests that galaxy morphology is partially driven by the large-scale anisotropic environment.

In the standard paradigm, the angular momentum (or spin) of proto-haloes is at linear order induced by the misalignment between the inertia tensor of the proto-halo and the tidal tensor in its surroundings (Hoyle 1949; Peebles 1969; Doroshkevich 1970; White 1984; Catelan & Theuns 1996; Crittenden et al. 2001, see also Schäfer 2009, for a review). At later stages, as the proto-haloes decouple from cosmic expansion and collapse into virialised structures, strongly non-linear processes may impact galaxies' angular momentum distribution (Porciani, Dekel & Hoffman 2002a, b). For instance, galactic outflows can redistribute angular momentum within the inner parts of galaxy haloes (Danovich et al. 2012), and increase the angular momentum of discs via wind recycling (Brook et al. 2011; Christensen et al. 2016).

Since the cosmic web is shaped by the same gravitational tidal field responsible for the acquisition of the net angular momentum of systems forming and evolving within, a correlation between the large-scale structure and the spin of haloes is directly expected from tidal torque theory (TTT). By revisiting TTT in the context of such anisotropic environment (filaments embedded in walls), Codis, Pichon & Pogosyan (2015b) showed that the constrained misalignment between the tidal and the inertia tensors in the vicinity of filament-type saddle points is able to explain the relative angular momentum distribution with respect to the cosmic web. In particular, such conditional scale-dependent tides imply a spin aligned with filaments for low mass haloes, and a perpendicular spin

★ E-mail: kat@roe.ac.uk

orientation for more massive haloes. This conditional TTT agrees with findings seen in haloes from cosmological *N*-body simulations (e.g. Aragón-Calvo et al. 2007; Hahn et al. 2007; Codis et al. 2012; Trowland, Lewis & Bland-Hawthorn 2013; Wang & Kang 2017; Ganeshaiah Veena et al. 2018).

A key prediction of the conditional TTT is thus that the spin orientation with respect to the embedding filament flips from low to high mass galaxies. This mass dependent flip of the spin can be understood qualitatively in the context of the dynamics of large-scale cosmic flows and mass accretion history of haloes within the anisotropic large-scale structure. The first generation of haloes formed in vorticity-rich filaments, and are thus expected to have their spin aligned with their embedding filament. At later stages, as the flow along filaments also shell-crosses, haloes flowing towards nodes of the cosmic web convert their orbital angular momentum into a spin perpendicular to the filament axis as they merge and grow in mass (e.g. Codis et al. (e.g. Codis et al. 2012; Welker et al. 2014; Kang & Wang 2015; Laigle et al. 2015; Codis et al. 2015b; Wang & Kang 2017, 2018)

All these processes affect galaxy spin alignments as well, but with a caveat – baryon specific effects (e.g. gas inflows, stellar and black hole-driven gas outflows, cooling and heating, instabilities, etc.) are additionally expected to impact their angular momentum. As a result, the relative spins of galaxies and their host haloes can show significant misalignments, depending on redshift, mass, or the central/satellite nature of the host (see e.g. Tenneti et al. 2014; Velliscig et al. 2015; Chisari et al. 2017). Due to the complexity of the processes involved in the formation and evolution of galaxies, our understanding of the details of galaxy-spin alignment is best examined in large-scale hydrodynamical simulations capable of capturing these highly non-linear processes.

Hahn, Teyssier & Carollo (2010) performed the first study addressing the spin alignment of galaxies with respect to their large-scale environment by analysing a sample of $\sim$ 100 disc galaxies in the region of a large-scale filament resimulated using the 'zoom-in' technique with adaptive mesh refinement (AMR) code RAMSES (Teyssier 2002). With the caveat of a limited statistical significance due to small number statistics, this work reported that the most massive disc galaxies at all redshifts tend to be aligned with the direction of the filament. Using the large-scale simulation HORIZON-AGN (Dubois et al. 2014) employing the same numerical technique, Codis et al. (2018) analysed galaxy spin orientation with respect to filaments and walls of the cosmic web inside of a comoving 100 Mpc h^{-1} cosmological volume. This work extended the previous study of Dubois et al. (2014) to a full cosmic evolution down to $z = 0$ and also considered an additional cosmic web environment, the walls. It confirmed the existence of a galaxy spin transition from parallel to perpendicular with respect to the filaments' direction, and analogously with respect to walls. Overall, blue or rotation-supported galaxies were found to dominate the alignment signal at low stellar mass, while red or dispersion-dominated galaxies tend to show a preferential perpendicular alignment. Similar conclusion regarding galaxy mass and colour dependence of the alignment signal with respect to filaments was reported by Wang et al. (2018) analysing the ILLUSTRIS-1 simulation (Vogelsberger et al. 2014), using the moving mesh code AREPO (Springel 2010). In contrast, Ganeshaiah Veena et al. (2019) recently reported a propensity of galaxies for perpendicular alignment with their host filaments at all masses with no sign of a spin transition. This work made use of the EAGLE simulation (Schaye et al. 2015), based on an updated version of the smoothed particle hydrodynamics (SPH) based galaxy formation code GADGET (Springel 2005). Similar non-detection of spin transition for galaxies was also reported by Krolewski et al. (2019) in another SPH-based simulation MASSIVE-BLACK II (Tenneti et al. 2014). It has been noted that the hydrodynamic methodology may play a role in spin studies, as AMR codes can suffer from 'grid locking' where disc evolution is compromised by the imposed Cartesian grid, while SPH has difficulties controlling the amount of spurious shear viscosity in rotating discs. Hence, the existence and sense of a 'spin flip' in alignment between low and high mass galaxies remains controversial.

A complicated picture is also found on the observational side. When studying the spin alignment of disc galaxies with respect to the filaments of the cosmic web, some groups find preferentially parallel orientation for spirals (Tempel, Stoica & Saar 2013; Tempel & Libeskind 2013), Scd types (Hirv et al. 2017), or both red and blue galaxies (Zhang et al. 2013), while others report either a tendency for a perpendicular orientation for spirals (Lee & Erdogdu 2007; Jones, van de Weygaert & Aragón-Calvo 2010; Zhang et al. 2015) and Sab galaxies (Hirv et al. 2017), or even no signal at all (Pahwa et al. 2016; Krolewski et al. 2019). There seems to be a much better agreement for elliptical/S0 galaxies, which are found to have their spin (or minor axis) perpendicular to their host filaments' direction, in line with results of shape measurements (e.g. Okumura & Jing 2009; Joachimi et al. 2011; Singh, Mandelbaum & More 2015; Chen et al. 2019; Johnston et al. 2019).

Studies regarding the spin alignment of galaxies within walls of the cosmic web lead to similarly contradictory conclusions. While some works reveal a tendency for spirals to have their spins aligned with the Local Supercluster plane (Flin & Godlowski 1986, 1990; Navarro, Abadi & Steinmetz 2004), the shells of the largest SDSS and 2dFGRS[1] cosmic voids (Trujillo, Carretero & Patiri 2006), or the so-called W-M sheet in the vicinity of the Virgo Cluster and the Local Void (Lee, Kim & Rey 2018), others report on the perpendicular orientation (Flin & Godlowski 1990; Varela et al. 2012; Zhang et al. 2015) or detect no signal (Slosar & White 2009; Tempel & Libeskind 2013). For elliptical galaxies, only a weak correlation has been detected between their minor axes and the normal to the sheet (Tempel & Libeskind 2013). There is currently no consensus to explain the differences seen among these various observations.

The method used to trace and quantify the cosmic web may play a crucial role in these measurements. Filament finding algorithms have a long history, with early attempts relying on the moment of inertia tensor (Dave et al. 1997), or Morse theory (Novikov, Colombi & Doré 2006) to define the local filament direction. In the last decade, various filament tracers have been developed (see Libeskind et al. 2018, for a comparative study of various cosmic web extraction techniques) which make distinct assumptions and deal differently with the range of probed scales, and thus lead to substantial diversity in some of the extracted properties of the cosmic web. Consequently, the efficiency of these estimators may impact our ability to quantify alignment signals (Welker et al. submitted). Hence, it is important to define the cosmic web in a way that is uniform and consistent, via a method that can be equally applied to observations in order to conduct fair comparisons to models.

This work studies the orientation of the spin of galaxies with respect to filaments and walls of the cosmic web, relying on a new large-scale hydrodynamical simulation SIMBA (Davé et al.

[1]Two Degree Field Galaxy Redshift Survey (2dFGRS; Colless et al. 2001) and the Sloan Digital Sky Survey (SDSS York et al. 2000).

2019). Our focus is first on the mass dependent flip of the spin, and its evolution in the redshift range $0 \leq z \leq 2$, for which contradictory results exist. Next, the alignment signal is investigated at $z = 0$ as a function of the internal properties of galaxies, namely their morphology, specific star formation rate (sSFR), HI mass and central/satellite dichotomy, and as a function of external properties, such as galaxies' halo mass and filaments' density. We also extend the recent studies of the spin alignment of galaxies with respect to the walls of the cosmic web. This investigation builds on previous work in several aspects. The SIMBA simulation employs a different hydrodynamic solver (a Meshless Finite Mass, or MFM, scheme) as opposed to SPH or AMR codes used for these studies (e.g. there is no shear viscosity in MFM), which allows the evolution of an equilibrium disc for many rotation periods without numerical fragmentation or grid locking (Hopkins 2015). SIMBA also includes a novel implementations of feedback from active galactic nuclei (AGNs) and star formation that results in comparably good or better agreement with a wide range of global galaxy properties (Davé et al. 2019) compared to state-of-the-art galaxy formation simulations. Finally, by using the same DISPERSE code to define the cosmic web as in Codis et al. (2018) and including orientation relative to walls, we can straightforwardly compare to those results, and eventually to observations, as we will do in future work.

The outline of this paper is as follows. Section 2 presents some of the main aspects of the SIMBA simulation and briefly describes how the DISPERSE algorithm is used in order to identify filaments and walls of the cosmic web. Section 3 investigates the alignments of spins of haloes with filaments and walls together with their redshift evolution. The results on the alignment of the spin of galaxies with respect to filaments and walls and their redshift evolution are reported in Section 4. In particular, we investigate the dependence of the alignment signal on the internal properties of galaxies such as their stellar mass, star formation activity, and their HI content. Section 5 is dedicated to the dependence of the spin-filament orientation of galaxies on environment, parametrized by the mass of their host halo, the central/satellite dichotomy and density of their host filaments. Finally, Section 6 concludes. The statistical significance quantified by Kolmogorov–Smirnov (KS) tests for the Figures is given in Appendix B.

Throughout this paper, by log, we refer to the 10-based logarithm.

2 VIRTUAL UNIVERSE

We first describe our virtual universe and the analysis tools we use to trace filaments, identify galaxies and measure their physical properties.

2.1 The Simba simulation

This work makes use of the SIMBA simulation (Davé et al. 2019) to follow galaxy and structure formation across cosmic time. SIMBA is a new large-scale cosmological hydrodynamical simulation built on the MUFASA suite (Davé, Thompson & Hopkins 2016), and is seen to successfully reproduce many observables, such as galaxy stellar mass functions at $z = 0 - 6$, the stellar mass star formation rate main sequence, HI and H_2 galaxy gas fractions, the mass-metallicity relation at $z = 0 - 2$, star-forming galaxy sizes, hot gas fractions in massive haloes, and galaxy dust properties at $z \sim 0$ (Davé et al. 2019). A full description of this simulation can be found in Davé et al. (2019); here we summarise only some of its main features relevant to this work.

SIMBA was run using the Meshless Finite Mass version of the GIZMO code (Hopkins 2015), a multimethod gravity plus hydrodynamics code based on GADGET-3 (Springel 2005). The SIMBA run used in this work follows the evolution of 1024^3 dark matter particles and 1024^3 gas elements in a volume of $(100\ h^{-1}\ \mathrm{Mpc})^3$. The simulation begins at $z = 249$ assuming a standard Lambda cold dark matter cosmology compatible with results from (Planck Collaboration et al. 2016), namely $\Omega_m = 0.3$, $\Omega_\Lambda = 0.7$, $\Omega_b = 0.048$, $H_0 = 68\ \mathrm{km\ s^{-1}\ Mpc^{-1}}$, $\sigma_8 = 0.82$ and $n_s = 0.97$. The minimum gravitational softening length for this run is 0.5 comoving h^{-1} kpc, the initial gas element mass is $1.82 \times 10^7\ \mathrm{M}_\odot$, and the dark matter particle mass resolution is $9.6 \times 10^7\ \mathrm{M}_\odot$.

Radiative cooling and photoionisation heating models, together with metal cooling and non-equilibrium evolution of primordial elements, make use of the GRACKLE-3.1 library (Smith et al. 2017). A spatially uniform ionising background, modified to account for self-shielding, is modelled following Haardt & Madau (2012). The HI content of gas particles is modelled self-consistently. Because significant amounts of HI can lie in an extended configuration beyond the star-forming region of galaxies, to assign HI to galaxies, all gas elements with HI fractions above 0.001 are considered, and assigned to the galaxy to which they are most gravitationally bound, i.e. its kinetic energy relative to the galaxy's center of mass velocity corrected for the potential energy from the galaxy at the gas element's location is minimised. The total HI mass of a galaxy is the sum of the HI masses of all associated particles.

SIMBA uses an H_2-based star formation prescription in a Jeans mass-resolving pressurized interstellar medium (ISM), following (Davé et al. 2016). The H_2 fraction is computed based on the prescription of Krumholz & Gnedin (2011). The model for stellar feedback uses decoupled metal-loaded two-phase galactic winds, with 30 per cent of wind particles being ejected 'hot'. SIMBA considers delayed feedback of metals and energy from Type Ia supernovae, asymptotic giant branch enrichment and wind heating.

Black hole growth is modelled via Bondi accretion from hot ($T > 10^5$K) gas and the torque-limited accretion model (Anglés-Alcázar et al. 2017) from cold gas. The model for AGN feedback uses kinetic bipolar outflows, with ∼1000 km/s winds at high Eddington rates and up to ∼8000 km/s jets at low Eddington rates, along with X-ray energy (Choi et al. 2012). The resulting population of quenched and star-forming galaxies and their black holes are generally in good agreement with observations (Davé et al. 2019; Thomas et al. 2019)

Identification of haloes is performed on the fly during the run using a 3D Friends-of-Friends (FoF) algorithm within GIZMO using a linking length of 0.2 times the mean interparticle distance. Identification of galaxies within haloes is done with a use of a post-processed 6-D FoF galaxy finder. The properties of galaxies and haloes are computed using the YT -based package CAESAR .

We define the spin of a galaxy as the angular momentum computed from its stellar particles, relative to the centre of mass of the stellar component. The angular momentum (or spin) $\mathbf{L}$ of galaxies is thus computed as

$$\mathbf{L} = \sum_{i=1}^{N_{\mathrm{stars}}} m_i \mathbf{x}_i \times \mathbf{v}_i, \tag{1}$$

where m_i, $\mathbf{x}_i$ and $\mathbf{v}_i$ and the mass, position and velocity of i-th stellar particle relative to the center of mass of the galaxy, respectively.

The morphology of galaxies is characterized by the kinematic ratio of their rotation to dispersion-dominated velocity, v/σ. This quantity is computed from the 3D velocity distribution of stellar particles of each galaxy. In order to define a set of cylindrical

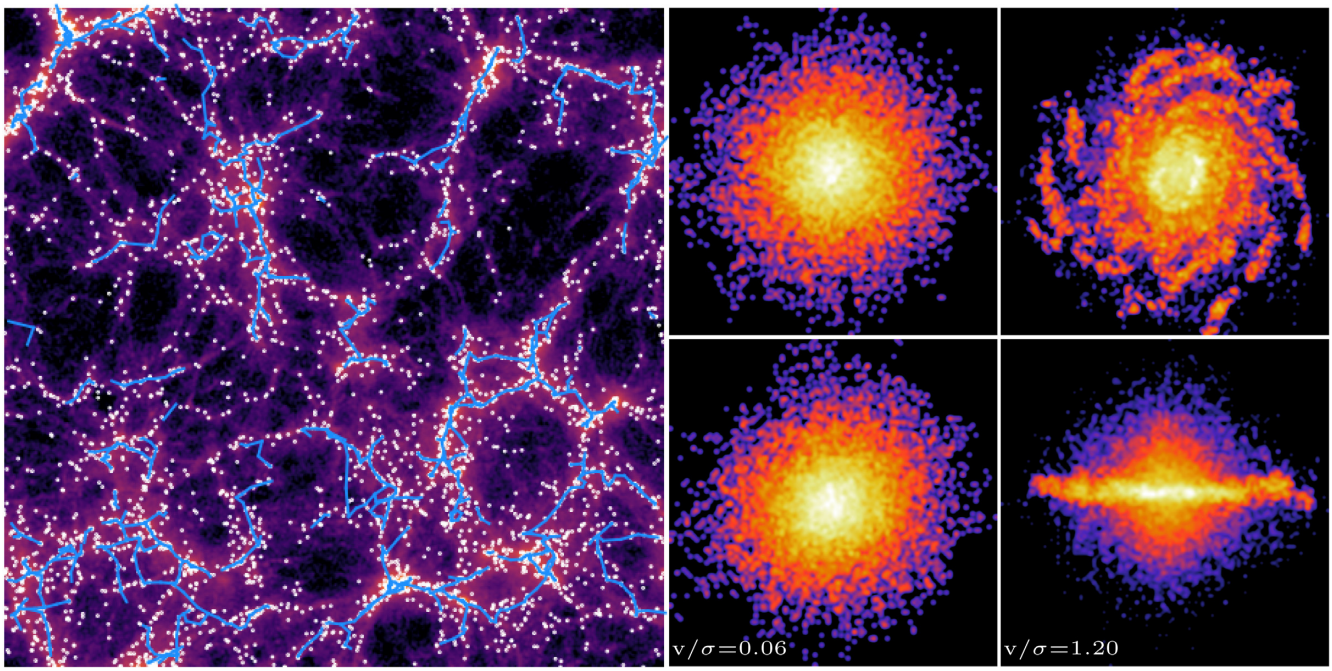

Figure 1. *Left:* A 2D projection of a 10 Mpc's simulation slice at $z = 0$. Galaxies (white circles) are overplotted on the gas distribution. The blue lines show the filaments as extracted by the DisPerSE code from the galaxy distribution using the persistent threshold of 3σ. *Right:* Examples of two galaxies of similar mass, $\log(M_\star/\mathrm{M}_\odot) \sim 11.2$, but with very different morphology as traced by their v/σ. The galaxy on the left is an elliptical with low v/σ, while the galaxy on the right has a disc-dominated morphology characterized by relatively high v/σ. For both galaxies face-on and edge-on projections are shown on top and bottom panels, respectively.

spatial coordinates (r, θ, z), the total angular momentum of stars is computed first and the z-axis is chosen to be oriented along the spin of galaxy. The velocity of each stellar particle is then decomposed into cylindrical components v_r, v_θ, v_z, and the rotational velocity of a galaxy v is defined as the mean of v_θ of individual stars. The average velocity dispersion of the galaxy $\sigma^2 = (\sigma_r^2 + \sigma_\theta^2 + \sigma_z^2)/3$ is computed using the velocity dispersion of each velocity component σ_r, σ_θ and σ_z. We note that this is not directly comparable to observational measures of v/σ, and here we simply use this quantity to separate rotation-dominated from dispersion-dominated systems.

2.2 Tracing the cosmic web

The filaments and walls of the cosmic web are extracted with the use of the publicly available code DisPerSE (Sousbie 2011; Sousbie, Pichon & Kawahara 2011).[2] DisPerSE is a geometric 3D ridge extractor, which identifies cosmic web structures with a parameter- and scale-free topologically motivated algorithm. It uses the notion of persistence that allows to select the retained structures on the basis of the significance of the topological connection between pairs of critical points (maxima, saddles).

For the purposes of this work, DisPerSE was run on the distribution of galaxies with a 3σ persistence threshold. It was checked that choosing higher threshold, such as 5σ, that would select topologically more robust structures, does not alter our results, in agreement with previous works that explored the dependence of the results on the persistence threshold in more details (Codis et al. 2018).

[2]http://www.iap.fr/users/sousbie/disperse/

Each galaxy is assigned its closest segment of the filaments, defined by a pair of points providing the direction of the filament for a given galaxy. The cosine of the angle between the spin of the galaxy and its closest filament, $\cos\theta$ is measured and used to assess the alignment with respect to the filamentary structure of the cosmic web. Values of $\cos\theta$ close to 1 mean that galaxy tends to have its spin aligned with the neighbouring filament, while values close to 0 mean that the spin is in the perpendicular direction with respect to the filament's axis. Similarly, each galaxy is assigned its closest triangle, the sets of which define the tessellation of the walls (2D analogue of the sets of segments defining filaments in 1D). The direction of the wall is defined by means of the normal vector to the triangle. The cosine of the angle between the spin of the galaxy and the normal to its closest wall, $\cos\theta$ is measured and used to assess the alignment with respect to the walls. Values of $\cos\theta$ close to 0 mean that galaxy tends to have its spin aligned with the neighbouring wall, while values close to 1 mean that the spin is perpendicular to the wall. In practice, in order to increase the statistics of the measured signal, each galaxy is assigned three closest filaments and walls, however, considering only one or two closest filaments and walls does not alter our results. In order to quantify the likelihood whether the measured alignments are consistent with being derived from a uniform distribution, a KS test was performed on each distribution. The corresponding probability, p_{KS}, for presented Figures can be found in Appendix B.

Fig. 1, left panel, shows the cosmic web identified by DisPerSE (blue lines), overlaid by the galaxy population (white dots), projected within a random 10 Mpc slice from the Simba simulation. The galaxies trace out the cosmic web as expected, with filaments and nodes clearly seen to follow the underlying gaseous cosmic web (shown as levels of purple). DisPerSE generally does a good job at identifying the filaments that one would trace out by eye

within that slice. Note that the DisPerSE skeleton is typically continuous, but in some places it goes outside the chosen slice, so the blue line terminates: in 3D, the skeleton continues beyond this slice.

The right-hand panel images show face-on (*top*) and edge-on (*bottom*) projections of the particle distribution for two massive galaxies, the left one randomly selected with low-v/σ, and the right one randomly selected among those with high v/σ. This shows that v/σ traces morphologies as expected, in that low v/σ galaxies are spheroidal while high v/σ ones are disc-like. We will examine galaxy spin alignments versus morphology later, where we will specifically use v/σ as a proxy to quantify morphology.

3 HALO SPIN ALIGNMENT

Let us start by studying the orientation of halo spin with respect to filaments and walls as a function of halo mass and redshift. We consider a sample made of all haloes with mass $M_h > 10^{10}\mathrm{M}_\odot$, in order to provide a more direct comparison to existing literature from both *N*-body and hydrodynamic simulations. It also sets the stage for understanding the trends seen in the spin alignments of galaxies. Indeed, while the details of the alignment between the spin of galaxies and the direction of their host filaments are still debated, there now seem to be a consensus in the literature on the halo spin–filament alignment. The spin of massive haloes is found to be preferentially perpendicular to filaments' direction and walls, while at the low mass end, haloes' spin tend to be aligned with their host filaments and walls, in both pure DM-only (e.g. Aragón-Calvo et al. 2007; Hahn et al. 2007; Sousbie et al. 2008; Codis et al. 2012; Ganeshaiah Veena et al. 2018) and simulations containing baryons (Dubois et al. 2014; Codis et al. 2018).

In order to extract the cosmic web for haloes, we run DisPerSE on the distribution of dark matter haloes with a 3σ persistence threshold. Fig. 2 shows the probability distribution function (PDF) of the cosine of the angle between the spin of haloes and the direction of their closest filament $\cos\theta_{f^h-h}$ (*left*), and the cosine of the angle between the spin of haloes and the normal of their their closest wall $\cos\theta_{w^h-h}$ (*right*) at redshifts 0, 1 and 2, in various halo mass bins as indicated. The mean cosine of the angle within each halo mass bin is indicated on each panel together with the probability for the KS test. There is a clear halo mass-dependent transition: low mass haloes tend to have their spin aligned with their closest filament and wall, while at high mass, their spin tend to be perpendicular to the direction to the closest filament's axis and wall, in particular at high redshifts. The transition mass where the spins are randomly oriented is around $\sim 10^{11.5} - 10^{12.5}\mathrm{M}_\odot$. This result from Simba is in general agreement with values reported in the literature, typically between $5\times10^{11}h^{-1}\mathrm{M}_\odot$ and $5\times10^{12}h^{-1}\mathrm{M}_\odot$ (Codis et al. 2012).

The amplitude of the signal, particularly the alignments with filaments, increases with increasing redshift. High-mass haloes at high redshift are quite likely to be perpendicular to their host filament. Low-mass haloes show less variation with redshift (see also Chisari et al. 2017, for a similar trend for the shape of dark haloes). The transition mass also varies with redshift, like the typical mass collapsing at that redshift, the so-called mass of non-linearity, which, as shown by Codis et al. (2012), increases with decreasing redshift as $1/(1+z)^{2.5}$ on those scales.

This quantitative agreement with previous work are expected, because baryonic effects do not play a major role in altering the spins of the haloes. However, moving to smaller scales where baryonic processes become more important, it is less obvious how the spin of the haloes relates to the spin of the stellar component of the galaxies, and in turn or independently how galaxy spins align with nearby filaments. This is what we examine next.

4 GALAXY SPIN ALIGNMENT

Simba forms and evolves galaxies, so we can study the spin alignments of the galaxies directly with respect to the filaments and walls of the cosmic web. For now, we focus on the spin of the stellar component; we will discuss the gas component spin later. Also, since galaxies have many other properties, we can examine the dependence of the spin alignment signal on various internal properties such as their stellar mass, their star formation activity as quantified by sSFR, their morphology as quantified by v/σ, their gas content as quantified by their neutral hydrogen (HI) mass, and their host halo mass. Furthermore, we will examine the dependence of the spin alignment on environmental factors, by studying spin alignments of galaxies separated into centrals and satellites and relative to the density of the nearest filament.

4.1 Stellar mass dependence

Let us start by quantifying the alignment of the spin of galaxies with respect to the filaments and walls as a function of galaxy stellar mass at different redshifts. In Simba, as in most cosmological models, the halo mass and galaxy mass are fairly tightly correlated, so in a simple model where the baryonic angular momentum reflects some fraction of that of the dark matter (as often assumed in semi-analytic models, for instance, see e.g. Benson & Bower 2010, and references therein), one would expect broadly similar trends as what we saw for haloes.

Fig. 3 shows the PDF of the cosine of the angle between the spin of galaxies and the direction vectors of their closest filament $\cos\theta_{f-g}$ (*left*), and the cosine of the angle between the spin of galaxies and the normal vectors of their their closest wall $\cos\theta_{w-g}$ (*right*) at redshifts $z=0$, 1 and 2, in different stellar mass bins. This is analogous to Fig. 2 for galaxies.

Similarly to what was seen for haloes, at all redshifts there exists a stellar mass dependent transition from the parallel to perpendicular alignment, such that low mass galaxies tend to have their spin aligned with their closest filament, while high mass galaxies their spin tend to be in the perpendicular direction to the closest filament. The transition mass between these two regimes is $M_* \approx 10^{10-10.5}\mathrm{M}_\odot$, which is approximately the stellar mass corresponding to the transition halo mass of $10^{11.5-12.5}\mathrm{M}_\odot$. This is more concisely shown on Fig. 4, displaying redshift and mass evolution of the mean cosine of the angle between the spin of galaxies and the direction vectors of their closest filament $\cos\theta_{f-g}$. Indeed, the transition mass at redshift 0 is roughly $10^{10.1\pm0.5}\mathrm{M}_\odot$. A lack of statistics does not allow us to detect a significant evolution of the transition mass with redshift.

Likewise, there is a clear mass dependence of the alignment with respect to walls at all redshifts. Low-mass galaxies tend to have their spins perpendicular to the normal of the walls, meaning that their spin lies in the plane of the wall. High-mass galaxies, conversely, have their spins preferentially aligned with the normal vector of the walls, therefore perpendicular to the plane of the walls (see also Appendix A1, Fig. A1).

While we do not have the ability to carry out a resolution convergence study with our current suite of simulations, we note that the spin-filament alignments were shown not to be strongly affected by the resolution in Horizon-AGN which is a comparably

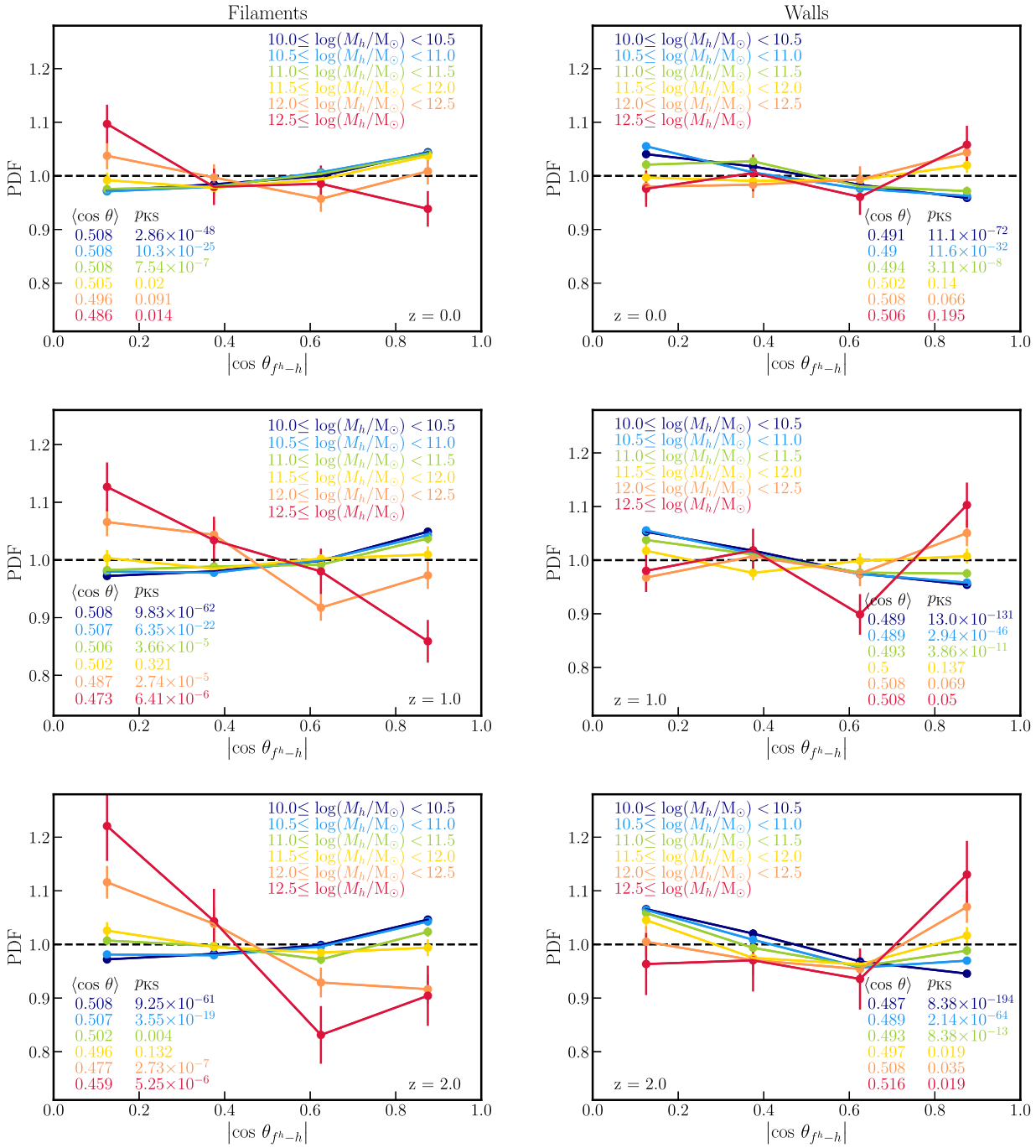

Figure 2. Alignment between the spin of haloes and filaments (*left*) and walls (*right*) in different halo mass bins, as labelled, at redshift $z = 0$ (*top row*), 1 (*middle row*) and 2 (*bottom row*). The cosmic web is reconstructed from the distribution of haloes with $\log(M_h/\mathrm{M}_\odot) \geq 10.0$. The horizontal black dashed line represents a random distribution. The error bars represent the Poisson noise. Note that the error bars are shown only to give an estimate of number of objects in individual bins. Statistical significance of the measured trends is assessed by performing the KS test, shown for each mass bin together with the mean $\cos\theta$. Massive haloes tend to have their spin perpendicular, and lower mass haloes parallel to their host filaments and walls.

large simulation (Codis et al. 2018) with similar resolution. We have also tested the impact of boundary effects of a catalogue[3] and found our results to be robust, which is encouraging in anticipation of measurements to be carried in bounded observational data sets.

In summary, SIMBA produces a subtle but statistically significant trend of galaxy spin alignment with nearby cosmic filaments and walls. The trend is mass-dependent, with low-mass galaxies having spins parallel to filaments and in the plane of walls, while high mass galaxies have spins perpendicular to filaments and the plane

[3]In practice, we tested whether running DISPERSE with and without the option of a periodic box has an impact on the obtained results.

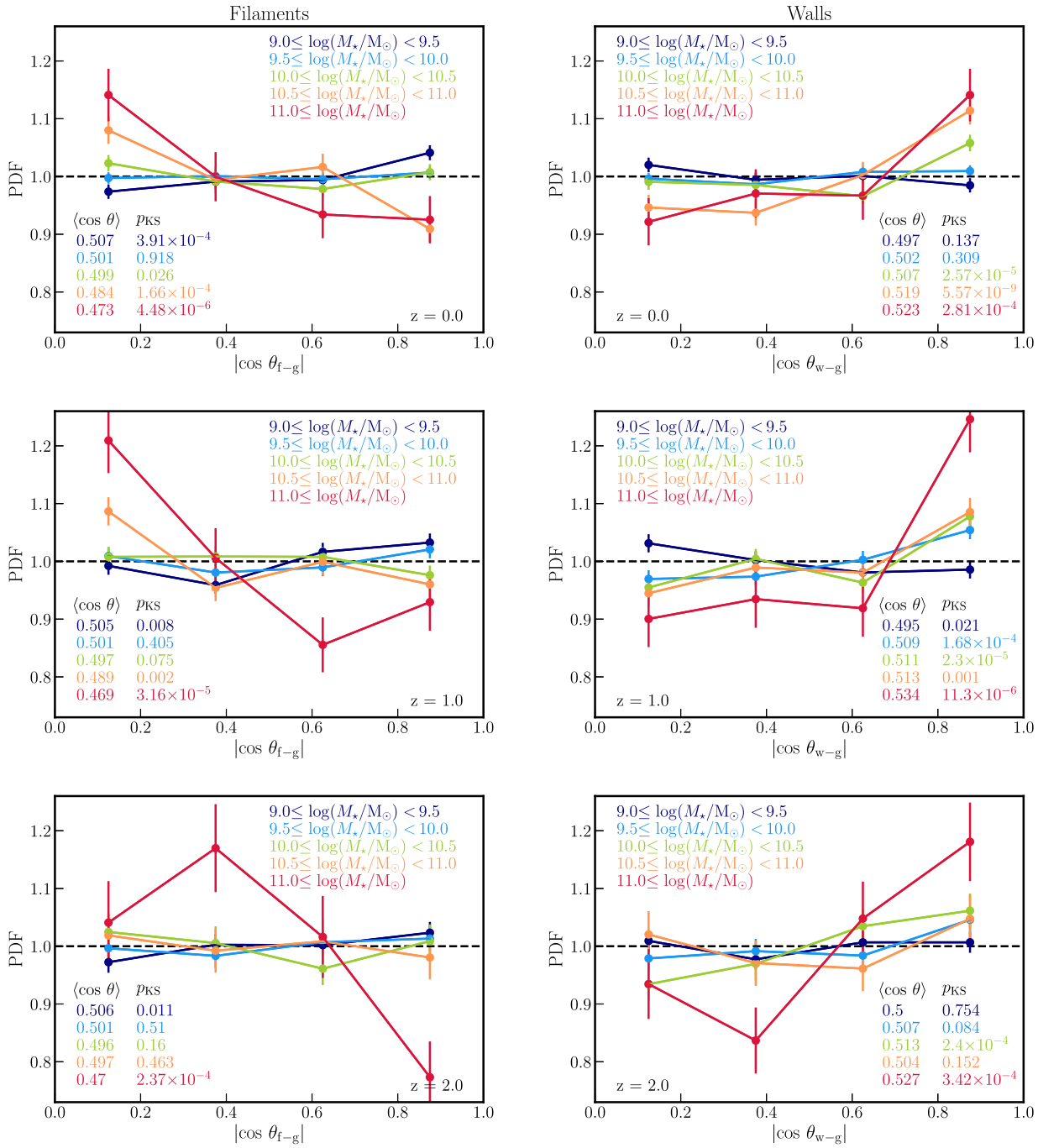

Figure 3. Alignment between the spin of galaxies and their closest filaments (*left column*) and walls (*right column*) in different stellar mass bins, as labelled, at redshifts $z = 0$ (*top row*), $z = 1$ (*middle row*) and $z = 2$ (*bottom row*). The error bars represent the Poisson noise. The horizontal black dashed line represents a random distribution. Massive galaxies tend to have their spin perpendicular to their host filaments, while at low mass, the spin of galaxies is preferentially aligned parallel to filaments. This stellar mass dependent flip of the spin is detected at all explored redshifts. Massive galaxies tend to have their spin perpendicular to their host walls at all redshifts. Preferential parallel orientation with respect to walls at low mass is clearly detected at $z = 1$, while for other redshifts, statistically significant signal ($p_{KS} < 0.05$) is obtained for galaxies with $M_\star \lesssim 10^{9.2}$ M$_\odot$.

of walls. The transition mass between these regimes where spins are randomly aligned is $\sim 10^{10}$M$_\odot$ (for filaments in particular, while it is less well constrained for walls). These results do not show a strong trend with redshift; in particular we do not see evidence for a stronger trend at high-z as we did for haloes. None the less, the overall trends generally follow that seen for haloes, showing that at least statistically, the galaxies seem to follow the spin alignment behaviour of their host haloes.

In the remainder of the paper, we focus on the filaments of the cosmic web, however, we note that as expected, qualitatively similar results are obtained when considering the walls.

4.2 Morphology dependence

Galaxy properties are globally dependent on stellar mass, with low-mass galaxies typically being star-forming, rotation-dominated, and

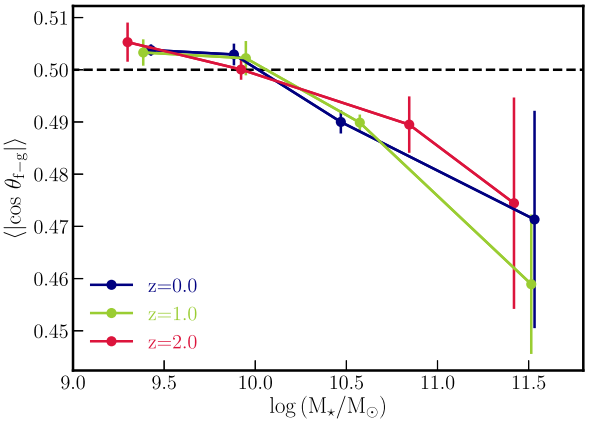

Figure 4. Mean alignment between the spin of galaxies and their host filaments as a function of $M_\star$ at redshifts z =2, 1 and 0, as labelled. The error bars represent the error on the mean among eight subcubes of the simulation. The stellar mass dependent flip of the spin (from parallel to filament at low mass to orthogonal at high mass) is detected at all explored redshifts.

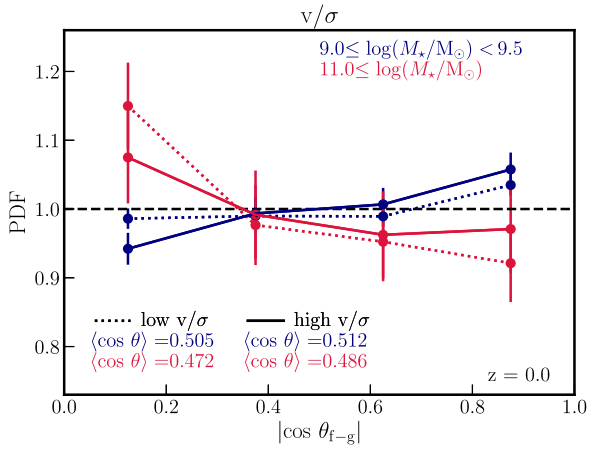

Figure 5. Alignment between the spin of galaxies and their closest filaments in the lowest and highest stellar mass bins, as labelled, at redshift $z = 0$ for galaxies with low (*dotted lines*) and high (*solid lines*) v/σ, corresponding to $v/\sigma < 0.4$ and $v/\sigma > 0.4$, respectively (see Table B3 for all $M_\star$ bins). The error bars represent the Poisson noise. The horizontal black dashed line represents a random distribution. The stellar mass dependent flip of the spin seen for the entire population of galaxies is detected for both the low and high v/σ populations. There is a hint for a tendency of galaxies with higher v/σ to dominate the parallel alignment signal at low stellar mass, while the perpendicular alignment signal tends to be dominated by galaxies with low v/σ.

(cold) gas-rich, while higher mass galaxies are the converse. Yet even at fixed stellar mass, galaxies display some diversity in these properties. Thus properties such as spin alignments may have a secondary dependence when split up by other properties besides stellar mass (Codis et al. 2018). In this section, we consider spin alignments of galaxies in various mass bins when further subdividing by galaxy morphology, which we quantify by its proxy v/σ into rotation-dominated ($v/\sigma > 0.4$) and dispersion-dominated ($v/\sigma < 0.4$) systems, with the demarcation chosen close to the median v/σ. With this, we can examine which morphological class of galaxies is responsible for driving the trends we see with $M_\star$ in the previous section.

Fig. 5 shows the resulting PDF of the cosines in high and low stellar mass bins for SIMBA galaxies at $z = 0$, for galaxies with low (*dotted lines*) and high (*solid lines*) values of v/σ, respectively. The intermediate mass alignments lie in between these extreme, and are mostly consistent with no alignment signal, so for clarity we do not show them.

The global trends are qualitatively similar for the rotation- and dispersion-dominated systems. Both show that at low mass, galaxy spins are aligned with filaments, while at high mass they are preferentially perpendicularly aligned. The strength of the trend is somewhat stronger in the high-mass dispersion-dominated systems; in this mass bin, the rotation-dominated systems show a weaker trend. Hence, the tendency for perpendicular alignment in massive galaxies appears to be driven by the dispersion-dominated systems.

Another depiction of this trend is shown in Fig. 8, upper left panel (a). Here, we show the mean alignment as a function of v/σ, over all galaxies. The red line shows the mean for all galaxies, and the dotted lines split these into centrals and satellites (discussed later). The only clear alignment signal happens for high-v/σ systems, which are aligned parallel to the filaments. The perpendicular alignment of low-v/σ systems is not evident when averaging over all galaxies.

In order to separate out the trend purely owing to morphology as opposed to that owing to a correlation between morphology and stellar mass, we examine the residuals in spin alignment versus morphology at a fixed $M_\star$, computed as the difference between $\cos\theta$ of a galaxy and the mean value at same $M_\star$. This is shown in the lower left panel (d) of Fig. 8. As clearly visible in the leftmost panels (a) and (d), which show the mean $\cos\theta_{f-g}$ as a function of v/σ and its residuals at fixed $M_\star$, the parallel alignment at high v/σ is not simply an effect of their typically low $M_\star$; morphology provides an additional driver in highly rotation-dominated systems that is not accounted for purely by the trend with $M_\star$. However, for the majority of galaxies with $v/\sigma \lesssim 1$, any existing trend is consistent with being purely driven by $M_\star$.

In summary, the parallel alignment signal with nearby filaments is driven by rotation-dominated galaxies, a trend that persists even after accounting for the underlying dependence of v/σ on $M_\star$. This is consistent with the idea that recent cosmological accretion drives galaxies to higher v/σ, and tends to occur with an angular momentum parallel to filaments, as expected from conditional tidal torque theory, and highlighted by Welker et al. (2014) for galaxies.

4.3 Star formation rate dependence

Analogously, we can examine the spin alignment signal when subdividing galaxies by their star formation activity. We split galaxies into star forming (blue) and quiescent (red) based on a cut in their sSFR at $\log(\mathrm{sSFR}/\mathrm{yr}^{-1}) = -11$, which is a canonical value for selecting quiescent galaxies. We note that SIMBA produces a quiescent galaxy fraction in quite good agreement with observations (Davé et al. 2019).

Fig. 6 shows the PDF of the cosine of the angle between the spin of galaxies and the direction vectors of their closest filament $\cos\theta_{f-g}$ for quiescent (*dotted lines*) and star-forming (*solid lines*) galaxies at redshift $z = 0$, in different stellar mass bins. As before, we only show the extreme $M_\star$ bins, as the intermediate mass bins show essentially no alignment signal.

Once again, the flip of the spin from low to high masses is seen, regardless of their star formation activity. Both quiescent and star-forming low-mass galaxies tend to have their spin aligned with the neighbouring filaments, while high mass ones have their spin preferentially in the perpendicular direction. This suggests that the

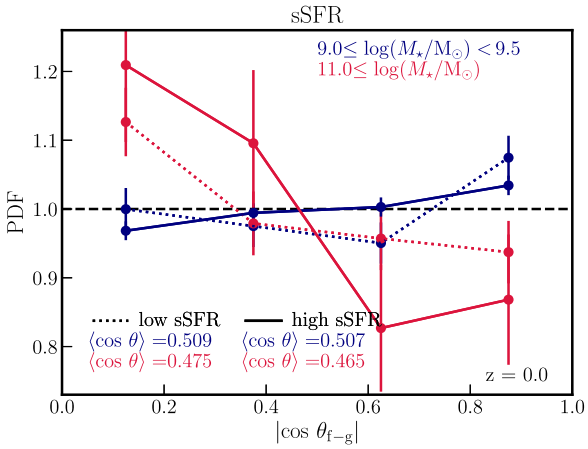

Figure 6. Alignment between the spin of galaxies and their closest filaments in the lowest and highest stellar mass bins, as labelled, at redshift $z = 0$ for quiescent galaxies (low sSFR , *dotted lines*) and star-forming galaxies (high sSFR , *solid lines*) based on the cut at $\log(\mathrm{sSFR}/\mathrm{yr}^{-1}) = -11$ (see Table B4 for all $M_\star$ bins). The error bars represent the Poisson noise. The horizontal black dashed line represents a random distribution. Both galaxy populations show a stellar mass dependent orientation of their spin with respect to filaments seen for the full galaxy sample with high (low) mass star-forming or quiescent galaxies having their spin preferentially perpendicular (parallel) to filaments.

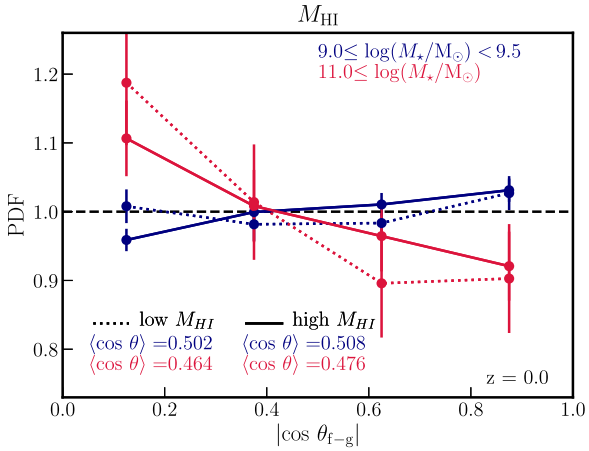

Figure 7. Alignment between the spin of galaxies and their closest filaments in the lowest and highest stellar mass bins, as labelled, at redshift $z = 0$ for galaxies with low (*dashed lines*) and high (*solid lines*) $M_{\rm HI}$, respectively, corresponding to split at $\log(M_{\rm HI}/\mathrm{M}_\odot) = 9.17$ (see Table B5 for all $M_\star$ bins). The error bars represent the Poisson noise. The horizontal black dashed line represents a random distribution. Stellar mass dependent flip of the spin seen for the entire population of galaxies is detected regardless of HI content of galaxies.

star formation activity of galaxies does not have a major impact on the alignment of galaxies.

Fig. 8 (panel b) presents this in a different way, as the mean alignment angle as a function of sSFR. This shows that there is a sSFR -dependent flip when the entire galaxy population is considered. The high mass galaxies that dominate the low sSFR end of the distribution are responsible for the perpendicular orientation of spin with respect filaments, while star-forming galaxies (high values of sSFR) dominate at low masses where the spins tend to be parallel with their host filament. In fact, this trend is entirely driven by the $M_\star$ dependence. This is evident from Fig. 8 (panel e), which shows the residuals of $\cos\theta_{f-g}$ at fixed $M_\star$, and demonstrates that even the small alignment signal disappears once $M_\star$ is fixed.

Hence star formation activity provides no discernible perturbation to the alignment trend over that expected from $M_\star$ alone. This is interesting because the alignment trend for highly rotation-dominated systems does not appear to translate simply into a similar dependence for high-sSFR galaxies. It appears morphology is more closely connected to spin than star formation activity in rotation-dominated systems.

4.4 HI mass dependence

The atomic neutral hydrogen (HI) mass represents a fuel reservoir for future star formation, and generally lies in the outskirts of galaxies. In SIMBA , the HI content is correlated with SFR even though the simulation assumes that stars form out of H_2 (Davé et al. 2019), hence HI provides a bridge between cosmological accretion occurring from the circumgalactic medium and star formation processes in the ISM. HI content is believed to be governed by relatively recent accretion, and is strongly dependent on environment (e.g. Rafieferantsoa et al. 2015; Crain et al. 2017; Kleiner et al. 2017; Crone Odekon et al. 2018). In the context of galaxy spin acquisition, low mass galaxies were suggested to build their spin in the vorticity-rich vicinity of filaments, via gas-rich infall (Laigle et al. 2015; Welker et al. 2018). One might therefore expect the alignment signal to be stronger for HI rich galaxies. Here, we examine this in SIMBA .

Fig. 7 shows the filament alignment angle PDF for $z = 0$ galaxies with high (*dotted lines*) and low (*solid lines*) HI content at redshift $z = 0$, showing the two extreme stellar mass bins. As we have seen with other quantities, regardless of HI content, low mass galaxies tend to have their spin parallel, with the signal being dominated by galaxies with high HI mass, and high mass galaxies perpendicular to their host filament.

Fig. 8 (panel c) displays the mean cosine of the angle between the spin of galaxies and the direction vectors of their closest filament $\cos\theta_{f-g}$ as a function of HI mass for all galaxies with some content of neutral hydrogen (87 per cent of SIMBA galaxies at $z = 0$ contain HI). Galaxies with low HI mass tend to have their spin preferentially perpendicular to filaments' direction, while galaxies with high HI mass are more likely to be aligned with the axis of their host filament. The transition HI mass where the spin flips is at $M_{\rm HI} \approx 10^{9.5}\mathrm{M}_\odot$.

The interesting question then is whether the HI dependence is simply a reflection of the correlation between $M_{\rm HI}$ and $M_\star$. To examine this, we also compute the residuals of the cosine of the angle between the spin of galaxies and the direction vectors of their closest filament $\cos\theta_{f-g}$ as a function of HI mass at fixed stellar mass, as shown in Fig. 8 (panel f).

Galaxies with high HI content tend to be more aligned with their host filaments compared to average population at same stellar mass, while at low HI mass they are more likely to have their spin perpendicular. The trend is not markedly different from the panel above, showing that the trend with HI still exists at a fixed $M_\star$, and hence is not driven by the $M_\star$ alignment dependence.

Thus it appears that the spin alignment of galaxies is impacted specifically by neutral hydrogen content. Interestingly, despite an overall correlation between HI and SFR in SIMBA (Davé et al. 2019), the spin alignment dependence on these two properties are markedly different. This is consistent with the suggestion that the alignment of spin with the local filament is driven by relatively recent accretion

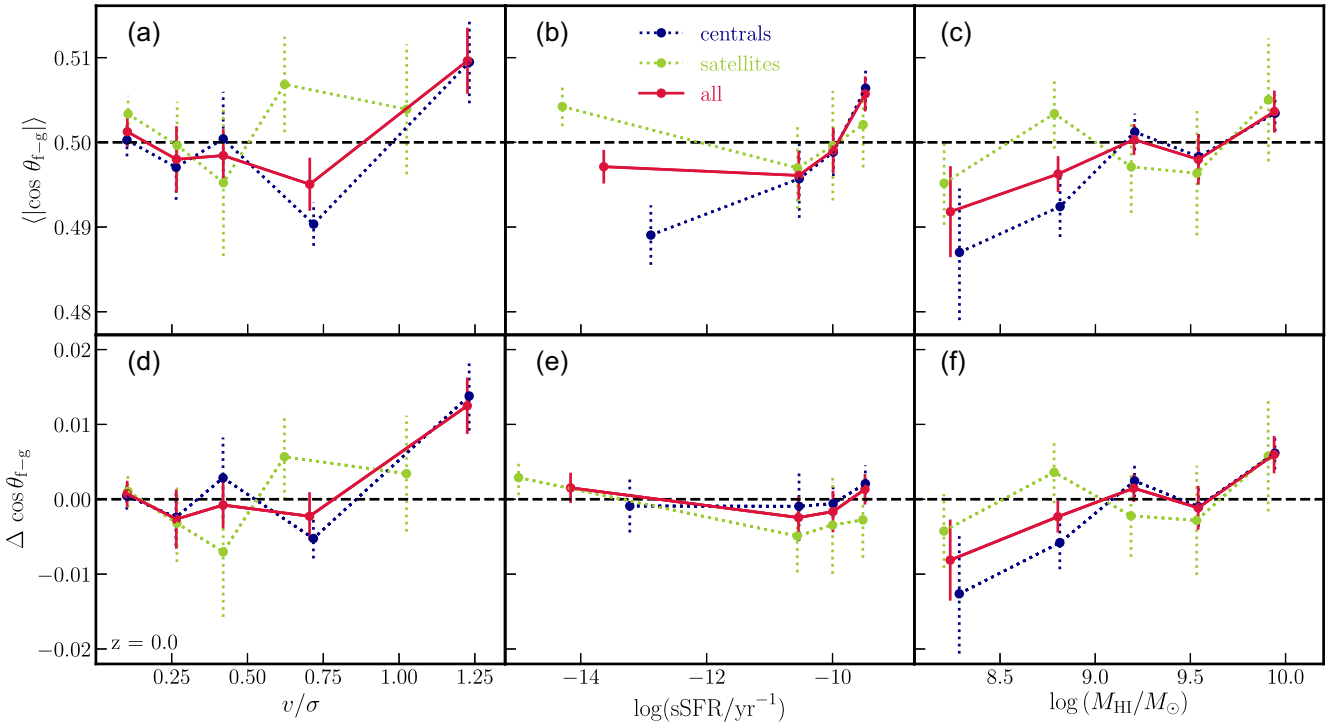

Figure 8. *Top row:* Mean alignment between the spin of galaxies and filaments as a function of v/σ (*left*), sSFR (*middle*) and HI mass (*right*) of galaxies at $z = 0$. The error bars are computed as in Fig. 4. Galaxies with high v/σ , sSFR and HI mass tend to align their spin with the filament's axis. A clear perpendicular orientation of the galaxies' spin with respect to their host filament is seen for galaxies with low HI content and for quenched centrals (with $\log(\mathrm{sSFR}/\mathrm{yr}^{-1}) \leq -11$). *Bottom row:* Residuals of the cosine of the angle between the spin of galaxies and the direction vectors of their closest filament $\cos\theta_{f-g}$ at fixed $M_\star$. Parallel spin-filament orientation of galaxies is clearly dominated by disc-dominated galaxies (with high v/σ), while all trends seen as a function of sSFR are entirely driven by $M_\star$. The strongest residuals are found for HI mass, with the parallel alignment being dominated by galaxies with high HI content, while galaxies with low HI mass are driving the perpendicular orientation.

spinning up the outskirts of galaxies (Pichon et al. 2011), which may not immediately increase the SFR.

5 IMPACT OF LOCAL AND GLOBAL ENVIRONMENT

The results from the previous section, particularly for HI, suggest that anisotropic accretion from the environment plays a specific role in the spin alignment of galaxies and their host filaments (beyond that expected from their host dark halo). In this section, we examine the environmental dependence in more detail on small and larger scales, by considering the host halo mass, the density of the nearest filament, and how spin alignment depends on whether a galaxy is a central or a satellite.

5.1 Halo mass dependence

We have examined the spin alignment of all haloes in Section 3. We now focus on the spin alignment of galaxies split by their host halo mass, as a proxy for the depth of the local potential well, to ascertain if it provides an important secondary effect, beyond $M_\star$, on spin alignments.

Fig. 9 shows the PDF of the cosine of the angle between the spin of galaxies and the direction vectors of their closest filament $\cos\theta_{f-g}$ at redshift $z = 0$ for galaxies living in low (*dotted lines*) and high (*solid lines*) mass haloes. The value used to split galaxies corresponds to the median halo mass, and we consider only the main halo for each galaxy, not the subhalo. Because of

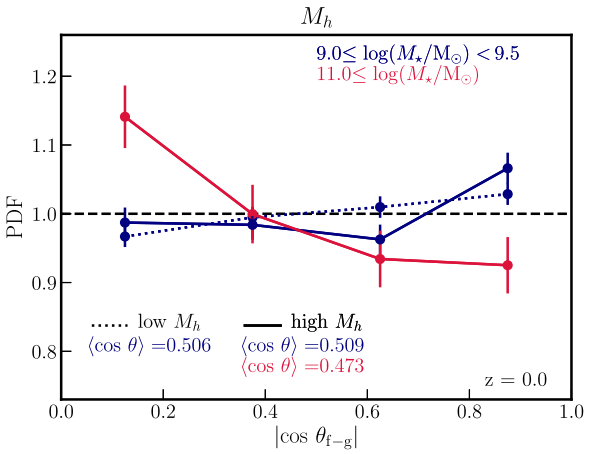

Figure 9. Alignment between the spin of galaxies and their closest filaments in different stellar mass bins, as labelled, at redshift $z = 0$ living in low (*dotted lines*) and high (*solid lines*) mass haloes (see Table B9 for all $M_\star$ bins). The value used to split galaxies corresponds to the median halo mass $10^{11.9}$ $M_\odot$. Note that only bins containing more than 100 galaxies are shown. The error bars represent the Poisson noise. The horizontal black dashed line represents a random distribution. Low-mass galaxies tend to align their spin in the direction of their host filament in both low and high-mass haloes. High mass galaxies are primarily found in massive haloes, where their spin is preferentially orthogonal to filaments. The parallel alignment at low stellar mass tend to be dominated by galaxies of high-mass haloes.

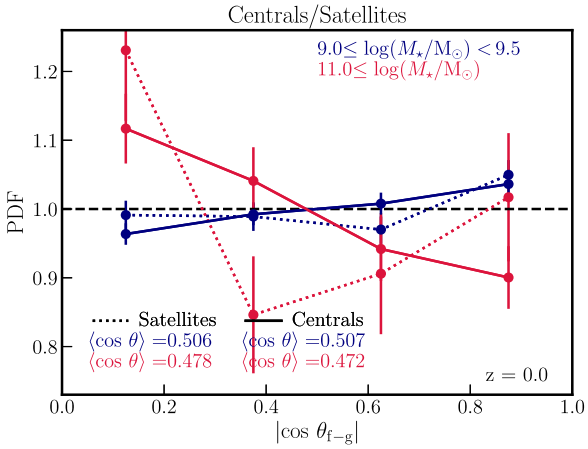

Figure 10. Alignment between the spin of galaxies and filaments in different stellar mass bins, as labelled, for satellites (*dotted lines*) and centrals (*solid lines*) at redshift $z = 0$ (see Table B7 for all $M_\star$ bins). The error bars represent the Poisson noise. The horizontal black dashed line represents a random distribution. Both central and satellite galaxies show similar alignment signal as the entire galaxy population. However, centrals tend to show stronger alignment signal compared to satellites at the same mass in all stellar mass bins.

the underlying stellar-halo mass relation, very few galaxies with mass $\log(M_\star/\mathrm{M}_\odot) \geq 10.5$ live in low-mass haloes, therefore, the perpendicular alignment with respect to filaments' direction at high stellar mass is driven by galaxies living in massive haloes. However, at low stellar mass, galaxies both of high and low halo mass tend to have their spins aligned with the neighbouring filaments, with a signal stronger for massive haloes.

Fig. 14 (panel a) shows the mean cosine of the angle between the spin of galaxies and their host filaments as a function of host halo mass M_h. Only central galaxies show a clear halo mass dependent flip of the spin, with a transition mass roughly $\log(M_h/\mathrm{M}_\odot) \approx 11.8$. This is in the range of the transition mass for all haloes. Not surprisingly, due to the lack of a tight correlation between the $M_\star$ of satellites and their host halo mass, there no obvious transition for satellites.

Fig. 14 (panel d) shows the residuals of the cosine $\Delta \cos\theta_{\mathrm{f-g}}$ at fixed $M_\star$, as a function of M_h. This is consistent with zero for all galaxies, suggesting that the alignment signal is driven by $M_\star$, without any extra variation with the depth of the potential well.

5.2 Impact of the host: Central/Satellite

We saw in the previous section the satellites do not appear to be aligned with the larger host halo. In this section, we separately examine central and satellite spin alignments in various mass bins, in order to investigate the impact of the nature of the host on the measured spin alignments.

Fig. 10 shows the PDF of the cosine of the angle between the spin of galaxies and the direction vectors of their closest filament $\cos\theta_{f-g}$ for centrals and satellites separately at $z = 0$. Both galaxy populations show a stellar mass-dependent flip of their spin, with a tendency to be parallel and perpendicular at low and high mass, respectively. The trend for satellites at low $M_\star$ almost exactly mimics that of centrals, while at high masses satellites tend to show a slightly stronger perpendicular alignment signal than centrals. The origin of this transition is discussed in Welker et al. (2018) in terms of the kinematics of satellites building-up their spin via quasi-polar flows during their infall into a halo, and subsequently re-orienting their spin through mergers.

We examine this more directly in Fig. 11, which shows the alignment between the spin of centrals (*left*) and satellites (*right*) and the spin of their main halo in different bins of $M_\star$ at $z = 0$. Note that here we consider the absolute value of the cosine of the angle between the spin of galaxies and their main halo, therefore without taking into account the orientation of the spin vectors. Central galaxies have their spin aligned with the spin of their haloes at all masses, while the distribution for satellites is consistent with being random in all stellar mass bins. This is reflected in the mean cosine of the angle being consistent with an alignment of the spin of central galaxies and their host halo ($\langle\cos\theta\text{g-h}\rangle = 0.22 - 0.34$ in the various mass bins), while it shows little correlation between the spin of satellites and that of their parent halo ($\langle\cos\theta\text{g-h}\rangle = 0.03 - 0.05$). Hence only the central galaxies' spin are related to their halo's spin, while satellites show very little correlation with their host halo.

Another view of the central/satellite dichotomy is if we consider the alignment between the closest filament (obtained from the distribution of galaxies) and the host halo, as shown in Fig. 12 in various $M_\star$ bins. As expected, the centrals follow the host halo trends, with low-mass centrals being weakly parallel aligned, while

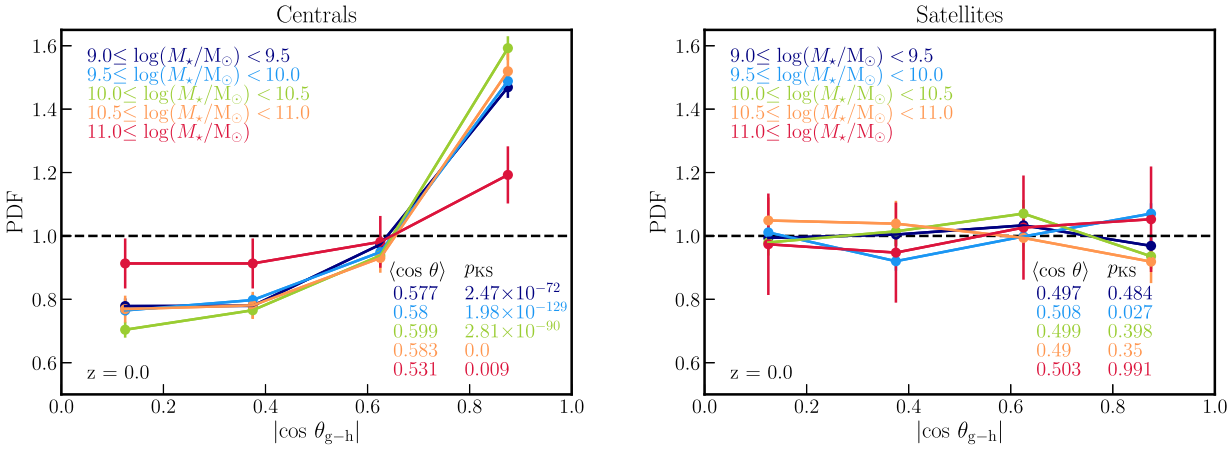

Figure 11. Alignment between the spin of galaxies and the spin of their main halo in different stellar mass bins, as labelled, at redshift $z = 0$ for centrals (*left*) and satellites (*right*). The error bars represent the Poisson noise. The horizontal black dashed line represents a random distribution. The spin of central galaxies is aligned with the spin of their host halo at all masses, while satellites show no correlation.

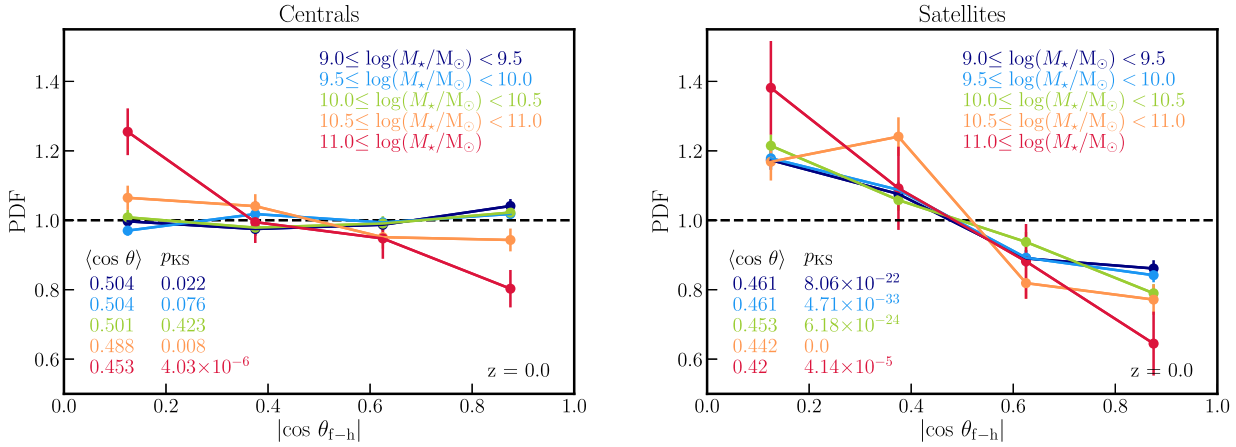

Figure 12. Alignment between the spin of haloes and galaxies' closest filaments in different stellar mass bins, as labelled, at redshift $z = 0$ for centrals (*left*) and satellites (*right*). The error bars represent the Poisson noise. The horizontal black dashed line represents a random distribution. The spin of haloes of central galaxies shows a similar mass dependent flip found for galaxies, such that host haloes of low mass centrals tend to have their spin aligned with the direction of central's closest filament, while at high mass they are perpendicular. Host haloes of satellites have their spin preferentially perpendicular to filaments' axes regardless of the mass of satellites. Recall that only galactic haloes are considered here, and their spin orientation is measured with respect to the same filamentary network as for galaxies, i.e. based on the distribution of galaxies.

high-mass ones are most strongly perpendicular. The interesting trend is for satellites, which shows them strongly perpendicular for all stellar masses. This partly reflects the halo occupancy distribution, in that the majority of satellites above a given mass live in large haloes, which tend to have perpendicular alignment overall. Indeed, the mean halo mass of satellites in all $M_\star$ bins is above 10^{13} $M_\odot$, and as shown in Fig. A2, such haloes have their spin in perpendicular direction with respect to filaments. This is also consistent with Aubert, Pichon & Colombi (2004) which found that the spin of subhalos lie perpendicular to the halo central separation vector, which typically corresponds to the local filament's direction.

Finally, we can return to Fig. 8 in order to examine the breakdown of the various second parameter spin alignment trends versus centrals and satellites (*dotted lines*). While the trends are broadly similar in alignment as a function of various galaxy properties, they are generally stronger for the central galaxies. Hence it appears that satellites tend to lose their spin alignment when they fall into another halo, as we saw earlier.

In summary, since satellites tend to be located in denser environments and in more massive haloes than centrals at the same stellar mass, the different trends for haloes of centrals and satellites seen in Figs 12 and A2 could be understood as a consequence of satellites residing near nodes where conditional TTT states that their spin should be orthogonal to the filament's direction.

5.3 Local and filaments' density dependence

Let us now investigate the local and filaments' density impact on the spin alignment of galaxies. In the framework of the TTT, the filament's (and wall's) density is expected to enhance the torque hence the alignment of the spin with respect to the large-scale anisotropic environment. Conversely, the node's density should also strengthen the perpendicular orientation at high mass.

Fig. 13 shows the PDF of the cosine of the angle between the spin of galaxies and the direction vectors of their closest filament $\cos\theta_{f-g}$ in the lowest (*dotted lines*) and the highest (*solid lines*) filament's density quartile at redshift $z = 0$. As expected, the alignment signal at low $M_\star$ is dominated by galaxies associated with dense filaments. Also as expected, at high $M_\star$, galaxies show statistically significant orthogonal orientation regardless of the filaments' density, since it is the relative node density which now torques it. Note that the same results are obtained for stellar mass-matched sub-samples of galaxies in low and dense environment, therefore these findings are not driven by low mass galaxies preferentially occupying low-density large-scale environments (resp. high mass and high density).

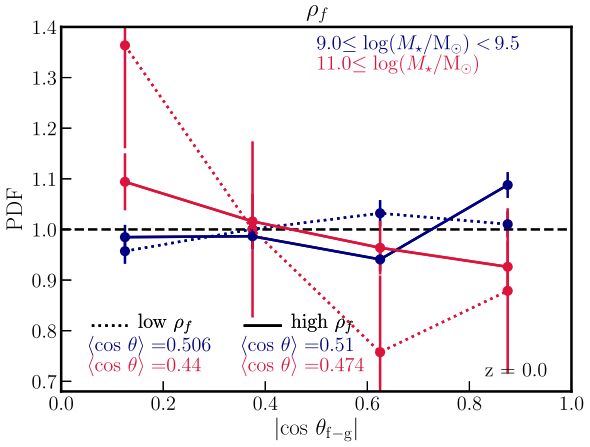

Figure 13. Alignment between the spin of galaxies and their closest filaments in the lowest and highest stellar mass bins, as labelled, at redshift $z = 0$ for the lowest (*dotted lines*) and highest (*solid lines*) filaments' density quartiles, corresponding to $\log(\rho/\mathrm{Mpc}^{-3}\mathrm{h}^{-3}) < -1.14$ and $\log(\rho/\mathrm{Mpc}^{-3}\mathrm{h}^{-3}) > 0.713$, respectively (see Table B8 for all $M_\star$ bins). The error bars represent the Poisson noise. The horizontal black dashed line represents a random distribution. Parallel alignment of the galaxy spin with respect to filaments is at low mass dominated by galaxies associated with high density filaments. The transition from parallel to perpendicular orientation of the spin occurs at higher stellar mass in high density environments.

This is consistent with the filament's density dependence of the alignments displayed on Fig. 14 (panel b), showing that the spin of galaxies associated with high-density filaments tend to be aligned with their axis, while there is a weak hint for galaxies having their spin perpendicular with respect to low-density filaments. This

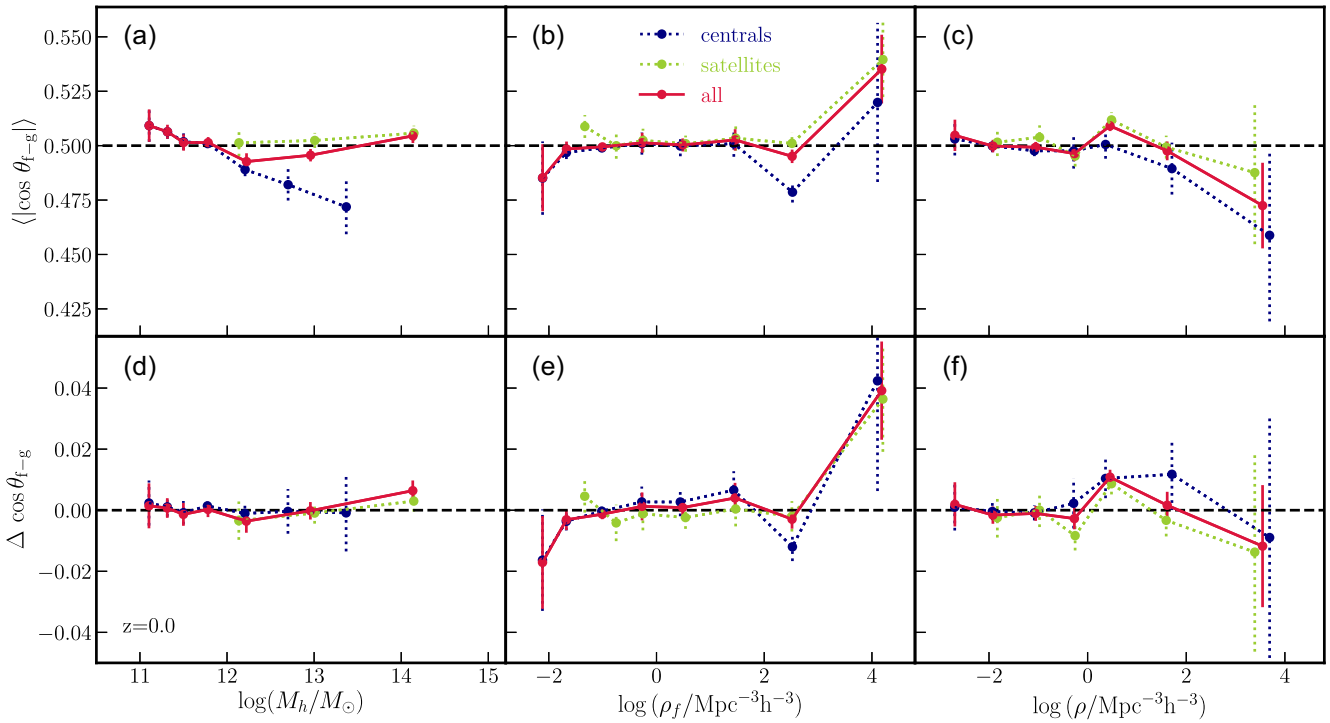

Figure 14. *Top row:* Mean alignment between the spin of galaxies and filaments as a function of halo mass M_h (*left*), host filament's density ρ_f (*middle*) and local density ρ (*right*) of galaxies at $z = 0$. The error bars are computed as in Fig. 4. Galaxies living in low-mass haloes tend to align their spin with the filament's axis, at intermediate halo mass they tend to have their spin in perpendicular direction, while at high halo mass only centrals continue to spin in perpendicular direction to the filaments. Galaxies associated with low-density filaments have their spin preferentially in perpendicular direction to filaments, while at high densities, there is a clear trend for galaxies to align their spin with their host filament. Galaxies living in high-density regions tend to have their spin in perpendicular direction to the filament's axis. *Bottom row:* Residuals of the cosine of the angle between the spin of galaxies and the direction vectors of their closest filament $\cos\theta_{f-g}$ at fixed $M_\star$. Trends seen as a function of halo mass are entirely driven by $M_\star$, while parallel spin-filament orientation of galaxies is clearly dominated by galaxies associated with high density filaments. Perpendicular spin-filament orientation of galaxies is marginally found to be dominated by galaxies living in highest density regions.

trend is not driven by stellar mass alone, as residuals at fixed $M_\star$ (Fig. 14, panel e) show similar trends suggesting, in particular, that the parallel spin-filament alignment signal is also driven by high density filaments, imposing stronger tides. Note that at low filaments' densities the weak tendency for the perpendicular spin-filament alignment at fixed $M_\star$ is still present, but the trend is weaker given the error bars.

Finally, we examine the spin alignment dependence on the local density at the galaxy's position, rather than the density of the nearest filament. Interestingly, Fig. 14 (panel c) shows that galaxies in high local density regions tend to have their spin preferentially perpendicular to their host filament, while in low local density regions, they tend to have their spin parallel. Residuals at fixed $M_\star$ are close to zero (Fig. 14, panel f), suggesting that stellar mass is driving the spin alignments, regardless of the local density.

The impact of the local density can be explained by differences in the position of these galaxies with respect to the cosmic web. Because of density gradients along filaments toward nodes, galaxies of the same filament that are further away typically have lower local density, compared to galaxies located in the vicinity of the nodes. Indeed, when considering the local density, the effect at high density is enhanced for galaxies in low $M_\star$ bin, while high mass galaxies are clearly perpendicular orientation, even at the highest densities. Thus the positive residuals at high filament's density are driven by galaxies further away from nodes. This is consistent with the interpretation that mergers (or equivalently accretion along the filaments), frequent in the nodes of the cosmic web, are driving the spin flips. We conclude that the exact 3D position of galaxies in the frame of the cosmic web is important to interpret the observed trends, as galaxies and their properties trace the geometry of the bulk flow within that frame (see e.g. Kraljic et al. 2019).

6 SUMMARY AND DISCUSSION

We have investigated the correlation between the spin orientation of galaxies and haloes and their large-scale anisotropic environment using the state-of-the-art cosmological hydrodynamical simulation SIMBA. The orientation of the angular momentum was measured relative to the direction of filaments and walls identified with the topological extractor DISPERSE. Our main focus was on its evolution as a function of stellar mass and redshift, as well as its dependence on secondary internal parameters such as morphology, HI content, star formation activity, and external parameters such as their halo mass, filament's density and the central/satellite dichotomy. Our principal findings are as follows.

(i) *Halos:* Halos show a strong alignment of their spin parallel to the filaments and walls at low masses and orthogonal at high masses, with a transition occurring at around $\log(M_h/\mathrm{M}_\odot) \approx 12.0 \pm 0.5$ at $z = 0$ for filaments, and at slightly higher mass for walls. This transition mass decreases with increasing redshift.

(ii) *Galaxies:* Galaxies' spin flip occurs at a corresponding mass of $\log(M_\star/\mathrm{M}_\odot) \approx 10 \pm 0.5$ for filaments, while the transition mass for walls is less well constrained.

(iii) *Morphology:* The perpendicular orientation is driven by high-mass dispersion-dominated systems, while rotation-dominated galaxies drive the parallel alignment at low masses. There is an additional weak trend due to morphology, beyond the trend established by $M_\star$ alone.

(iv) *Star formation:* Star-forming galaxies are preferentially parallel to filaments and quiescent galaxies tend to orient themselves perpendicularly, however this trend can be explained purely by its $M_\star$ dependence.

(v) *HI mass:* Interestingly, spin alignment is found to correlate significantly with HI content. Even at a given stellar mass, galaxies with high HI mass tend to align their spins with the axis of the filament while the spin of low HI-mass galaxies is more likely to be perpendicular to the direction of the closest filament. This suggests that recent accretion drives up both galaxy spin as well as HI content, and that the accretion appears to have an angular momentum that is parallel to the filament.

(vi) *Host halo mass:* Low mass galaxies align their spin to filaments in both low- and high-mass (main) haloes. High-mass galaxies are all found in high mass haloes, therefore they all display a preferential orthogonal orientation of their spin with respect to filaments. However, no additional dependence of the spin-filament orientation on the halo mass is detected beyond the $M_\star$ dependence. The spin of central galaxies and their haloes seem to be sufficiently coupled: there is no systematic bias in using galaxies (as a proxy for dark haloes) as tracers of spin alignment. The tight correlation between the $M_\star$ of centrals and their host halo's mass seems to be sufficient to explain the observed effect.

(vii) *Centrals/Satellites:* Central and satellite galaxies both show a stellar mass dependent flip of their spin with respect to filaments at $z = 0$. Due to the tight (main) halo mass–stellar mass correlation for centrals, this population of galaxies shows also a halo mass-dependent flip of their spin, with centrals living in low (high) mass haloes aligning their spin in parallel (perpendicular) direction to the filaments' axes. Spin-filament alignment for satellites does not show any correlation with the mass of their main halo. At fixed $M_\star$, no residuals in the alignment signal as a function of halo mass are detected, neither for centrals nor for satellites.

(viii) *Centrals/Satellites versus halo spin:* Central galaxies tend to align their spin with the spin of their host haloes at all stellar masses, while satellites show no correlation. Halos of centrals align their spin with the filaments at low stellar and halo mass, and have their spin perpendicular at high stellar and halo mass. Halos of satellites have their spin clearly perpendicular independently of stellar mass, and in all but the lowest halo mass bin.

(ix) *Local and nearby filaments' density:* The alignment signal at low $M_\star$ is dominated by galaxies of high density filaments, while at high $M_\star$, the spin of galaxies is orthogonal to filaments at all densities. As a result, the residuals at fixed $M_\star$ suggest that at low filaments' densities, galaxy spins tend to be orthogonal, and at high densities parallel to the host filaments. When considering instead the density at the location of galaxies, residuals at fixed $M_\star$ are close to zero, suggesting that stellar mass is enough to account for the observed spin flip.

The alignment of the spin of haloes with respect to filaments of the cosmic web has received a lot of attention in the past, in part to test predictions from tidal torque theory, and the canonical assumption used in e.g. semi-analytic models that the spin of the galaxy follows the direction of its host halo. In contrast, studies of the alignment of the *galaxy* spin in the context of large-scale structure have emerged only recently, motivated for example because intrinsic alignments are a source of contamination for weak-lensing-based dark energy surveys (Chisari et al. 2017).

Our results for haloes' spin showing a flip in spin orientation from low to high masses, and the corresponding transition mass, are in a good agreement with trends seen in both dark matter only simulations (e.g. Aragón-Calvo et al. 2007; Codis et al. 2012; Ganeshaiah Veena et al. 2018), and most hydrodynamical simulations (e.g. Codis et al. 2018; Ganeshaiah Veena et al. 2019). Analogously, the stellar mass dependent flip of galactic spin found in the present work is also consistent with findings of Welker et al. (2014), Codis et al. (2018) and Wang et al. (2018), at $z \leq 2$ and $z = 0$, respectively. While we did not test the specific role of mergers as in Welker et al. (2014), their results that mergers do not play a role in low-mass spin alignments is consistent with the importance of accretion as traced by HI content for driving the spin alignment in SIMBA. The lack of detection of a clear transition reported by Ganeshaiah Veena et al. (2019) was argued to be a consequence of the properties of the underlying filament, with galaxies in thinner filaments having their spins more likely perpendicular to the filament's axis, compared to galaxies of similar mass in thicker filaments. A straightforward interpretation of this result is the multiscale nature of the problem. At fixed halo mass, changing the thickness of filaments is equivalent to changing the smoothing scale defining the filament, hence changing the mass of non-linearity against which that mass must be compared.[4] Conditional TTT predicts that if it is below the corresponding mass of non-linearity (thick filament), the spin tends to be parallel, and if it is above, the spin is perpendicular. To confirm this, since filament thickness is not something that is topologically defined, hence not characterized using DISPERSE, we used the filament density as a proxy instead. With this proxy, our findings are consistent with conditional TTT predicting stronger impact of large-scale tides on the galaxy spin orientation in denser filaments.

Regarding the dependence of the spin-filament alignment on the internal properties of galaxies, our finding that the parallel alignment tend to be driven by galaxies with high v/σ (rotation-dominated galaxies) while the perpendicular alignment signal is dominated by low v/σ population (with elliptical morphologies) is in agreement with results of Codis et al. (2018). The dependence on star formation activity can be explained purely as a stellar mass effect, in qualitative agreement with Wang et al. (2018), when splitting galaxies into blue and red populations based on their $g - r$ colour. The stronger signal for morphology versus star formation activity suggests that spin is more directly related to the former.

Consistently with previous studies (e.g. Codis et al. 2018), the spin of satellites in SIMBA is found to be uncorrelated with the spin of their main halo, while the spin of centrals is much better correlated with that of their haloes. It was suggested by these authors that this may be an indication that satellites lose the memory of the filaments from which they emerged during virialisation. That said, we do find in SIMBA that satellites still show a stellar mass dependent flip, in tension with the findings of Codis et al. (2018) at low redshifts, showing no transition and no mass dependence. This may reflect a

[4]The denser the filament the thicker and therefore the larger the transition mass (see fig. 17 of Codis et al. 2015a) as it corresponds to the mass enclosed in the sphere of radius one-half of the radius of the filament. At fixed halo mass, the lighter the filament the more perpendicular the alignment. Alternatively and equivalently, if the halo is smaller than the quadrant of vorticity defined by its thickness, it will have its spin aligned with the filament (Laigle et al. 2015).

difference between these simulations in how long satellites retain memory of their original halo's spin, i.e. how much merging and harassment they undergo as satellites.

Interestingly, we find that the parent haloes of satellites have their spin clearly perpendicular to the filaments' direction, independently of their stellar mass. Given that satellites tend to live in more massive haloes than the centrals at the same stellar mass, this is a signature of the merger induced perpendicular orientation of halo spins at higher mass. Beyond the processes satellites undergo as they interact with their hosts and other satellites, they are also more likely to be influenced by strong AGN feedback from their massive central, potentially modifying their spin orientation. The implementation of the AGN feedback in the SIMBA simulation differs significantly from the prescription used in other simulations (e.g. ILLUSTRIS-1, EAGLE or HORIZON-AGN), as SIMBA always uses kinetic bipolar outflows for all black hole feedback. Conversely, the more spherical (thermal) feedback implemented in simulations such as EAGLE and for moderate-sized black holes in ILLUSTRIS-1 and HORIZON-AGN may more efficiently destroy the cosmic flows feeding satellites with angular momentum-rich cold gas, and building their own spin parallel to their embedding filaments (Dubois et al. 2012).

There has also been some controversy regarding hydrodynamics methodology. As it happens, the results of previous studies on spin alignments in cosmological hydrodynamical simulations seem to fall in two categories depending on the implemented numerical technique. Works using SPH simulations typically did not detect the mass dependent flip of the spin, in contrast to those analysing simulations using AMR codes. SIMBA employs an ALE-like (Arbitrary Lagrangian Eulerian) code for hydrodynamics, which is fully adaptive in a Lagrangian sense but uses a Riemann solver rather than smoothed pressures to compute forces, and does not include an artificial viscosity like SPH codes. Our results are more consistent with findings relying on AMR codes using the same cosmic web finder, indicating that (i) the details in modelling of hydrodynamics may play an important role in preserving the subtle interplay between the larger scale cosmic web and the internal dynamics of galaxies; and (ii) AMR grid locking cannot be the sole source of spin alignment at low mass. In addition, different algorithms used to identify the cosmic web may impact the quantitative signal of spin alignments with large-scale structure. Future comparisons to observations should strive to employ similar techniques, such as applying DISPERSE to galaxy redshift surveys.

Finally, our results are globally consistent with conditional tidal torque theory constrained to the vicinity of filaments and walls (Codis et al. 2015b). As this theory strictly applies to dark matter haloes only, finding qualitatively similar results for galaxies suggests that in spite of a variety of baryonic processes not accounted for in this theoretical framework, galaxies in fact continue to be impacted by the dynamics of the large-scale cosmic flows from which their haloes originated. Our results particularly highlight the correlation of spin alignment with respect to the HI content as further evidence for the role of the cosmic flows in feeding angular momentum-rich gas to young galaxies (Pichon et al. 2011; Stewart et al. 2011). This also suggests that HI could play an important role in identifying the expected orientation of galaxies in surveys where galaxy shapes are poorly resolved, such as in some upcoming weak lensing surveys with Large Synoptic Survey Telescope (LSST[5]).

[5]https://www.lsst.org/

ACKNOWLEDGEMENTS

The authors thank the anonymous referee for comments and suggestions that helped improve the presentation of the paper. SIMBA was run on the DiRAC@Durham facility managed by the Institute for Computational Cosmology on behalf of the STFC DiRAC HPC Facility. The equipment was funded by BEIS capital funding via STFC capital grants ST/P002293/1, ST/R002371/1 and ST/S002502/1, Durham University and STFC operations grant ST/R000832/1. DiRAC is part of the National e-Infrastructure. This work is partially supported by the Spin(e) grants ANR- 13-BS05-0005 (http://cosmicorigin.org) of the French Agence Nationale de la Recherche. We thank S. Rouberol for smoothly running the HORIZON cluster, hosted by the Institut d'Astrophysique de Paris, where some of the postprocessing was carried out, and T. Sousbie for DISPERSE . KK thanks Elisa Chisari, Sandrine Codis and Clotilde Laigle for fruitful comments and discussions. RD acknowledges support from the Wolfson Research Merit Award program of the U.K. Royal Society.

REFERENCES

Anglés-Alcázar D., Davé R., Faucher-Giguère C.-A., Özel F., Hopkins P. F., 2017, MNRAS, 464, 2840
Aragón-Calvo M. A., van de Weygaert R., Jones B. J. T., van der Hulst J. M., 2007, ApJ, 655, L5
Aubert D., Pichon C., Colombi S., 2004, MNRAS, 352, 376
Benson A. J., Bower R., 2010, MNRAS, 405, 1573
Brook C. B., Stinson G., Gibson B. K., Roškar R., Wadsley J., Quinn T., 2012, MNRAS, 419, 771
Catelan P., Theuns T., 1996, MNRAS, 282, 455
Chen Y.-C., Ho S., Blazek J., He S., Mandelbaum R., Melchior P., Singh S., 2019, MNRAS, 485, 2492
Chisari N. E. et al., 2017, MNRAS, 472, 1163
Choi E., Ostriker J. P., Naab T., Johansson P. H., 2012, ApJ, 754, 125
Christensen C. R., Davé R., Governato F., Pontzen A., Brooks A., Munshi F., Quinn T., Wadsley J., 2016, ApJ, 824, 57
Codis S. et al., 2015a, MNRAS, 448, 3391
Codis S., Pichon C., Devriendt J., Slyz A., Pogosyan D., Dubois Y., Sousbie T., 2012, MNRAS, 427, 3320
Codis S., Pichon C., Pogosyan D., 2015b, MNRAS, 452, 3369
Codis S., Jindal A., Chisari N. E., Vibert D., Dubois Y., Pichon C., Devriendt J., 2018, MNRAS, 481, 4753
Colless M. et al., 2001, MNRAS, 328, 1039
Crain R. A. et al., 2017, MNRAS, 464, 4204
Crittenden R. G., Natarajan P., Pen U.-L., Theuns T., 2001, ApJ, 559, 552
Crone Odekon M., Hallenbeck G., Haynes M. P., Koopmann R. A., Phi A., Wolfe P.-F., 2018, ApJ, 852, 142
Danovich M., Dekel A., Hahn O., Teyssier R., 2012, MNRAS, 422, 1732
Dave R., Hellinger D., Primack J., Nolthenius R., Klypin A., 1997, MNRAS, 284, 607
Davé R., Thompson R., Hopkins P. F., 2016, MNRAS, 462, 3265
Davé R., Anglés-Alcázar D., Narayanan D., Li Q., Rafieferantsoa M. H., Appleby S., 2019, MNRAS, 486, 2827
Doroshkevich A. G., 1970, Astrophysics, 6, 320
Dubois Y. et al., 2014, MNRAS, 444, 1453
Dubois Y., Devriendt J., Slyz A., Teyssier R., 2012, MNRAS, 420, 2662
Flin P., Godlowski W., 1986, MNRAS, 222, 525
Flin P., Godlowski W., 1990, Sov. Astron. Lett., 16, 209
Ganeshaiah Veena P., Cautun M., van de Weygaert R., Tempel E., Jones B. J. T., Rieder S., Frenk C. S., 2018, MNRAS, 481, 414
Ganeshaiah Veena P., Cautun M., Tempel E., van de Weygaert R., Frenk C. S., 2019, MNRAS, 487, 1607
Haardt F., Madau P., 2012, ApJ, 746, 125
Hahn O., Carollo C. M., Porciani C., Dekel A., 2007, MNRAS, 381, 41
Hahn O., Teyssier R., Carollo C. M., 2010, MNRAS, 405, 274

Hirv A., Pelt J., Saar E., Tago E., Tamm A., Tempel E., Einasto M., 2017, A&A, 599, A31
Hopkins P. F., 2015, MNRAS, 450, 53
Hoyle F., 1949, Problems of Cosmical Aerodynamics, Central Air Documents Office, Dayton, OH
Joachimi B., Mandelbaum R., Abdalla F. B., Bridle S. L., 2011, A&A, 527, A26
Johnston H. et al., 2019, A&A, 624, A30
Jones B. J. T., van de Weygaert R., Aragón-Calvo M. A., 2010, MNRAS, 408, 897
Kang X., Wang P., 2015, ApJ, 813, 6
Kleiner D., Pimbblet K. A., Jones D. H., Koribalski B. S., Serra P., 2017, MNRAS, 466, 4692
Kraljic K. et al., 2019, MNRAS, 483, 3227
Krolewski A., Ho S., Chen Y.-C., Chan P. F., Tenneti A., Bizyaev D., Kraljic K., 2019, ApJ, 876, 52
Krumholz M. R., Gnedin N. Y., 2011, ApJ, 729, 36
Laigle C. et al., 2015, MNRAS, 446, 2744
Lee J., Erdogdu P., 2007, ApJ, 671, 1248
Lee J., Kim S., Rey S.-C., 2018, ApJ, 860, 127
Libeskind N. I. et al., 2018, MNRAS, 473, 1195
Navarro J. F., Abadi M. G., Steinmetz M., 2004, ApJ, 613, L41
Novikov D., Colombi S., Doré O., 2006, MNRAS, 366, 1201
Okumura T., Jing Y. P., 2009, ApJ, 694, L83
Pahwa I. et al., 2016, MNRAS, 457, 695
Peebles P. J. E., 1969, ApJ, 155, 393
Pichon C., Pogosyan D., Kimm T., Slyz A., Devriendt J., Dubois Y., 2011, MNRAS, 418, 2493
Planck Collaboration et al., 2016, A&A, 594, A13
Porciani C., Dekel A., Hoffman Y., 2002a, MNRAS, 332, 325
Porciani C., Dekel A., Hoffman Y., 2002b, MNRAS, 332, 339
Rafieferantsoa M., Davé R., Anglés-Alcázar D., Katz N., Kollmeier J. A., Oppenheimer B. D., 2015, MNRAS, 453, 3980
Schäfer B. M., 2009, Int. J. Mod. Phys. D, 18, 173
Schaye J. et al., 2015, MNRAS, 446, 521
Singh S., Mandelbaum R., More S., 2015, MNRAS, 450, 2195
Slosar A., White M., 2009, J. Cosmology Astropart. Phys., 6, 9
Smith B. D. et al., 2017, MNRAS, 466, 2217
Sousbie T., 2011, MNRAS, 414, 350
Sousbie T., Pichon C., Colombi S., Novikov D., Pogosyan D., 2008, MNRAS, 383, 1655
Sousbie T., Pichon C., Kawahara H., 2011, MNRAS, 414, 384
Springel V., 2005, MNRAS, 364, 1105
Springel V., 2010, MNRAS, 401, 791
Stewart K. R., Kaufmann T., Bullock J. S., Barton E. J., Maller A. H., Diemand J., Wadsley J., 2011, ApJ, 738, 39
Tempel E., Libeskind N. I., 2013, ApJ, 775, L42
Tempel E., Stoica R. S., Saar E., 2013, MNRAS, 428, 1827
Tenneti A., Mandelbaum R., Di Matteo T., Feng Y., Khandai N., 2014, MNRAS, 441, 470
Teyssier R., 2002, A&A, 385, 337
Thomas N., Davé R., Anglés-Alcázar D., Jarvis M., 2019, MNRAS, 487, 5764
Trowland H. E., Lewis G. F., Bland-Hawthorn J., 2013, ApJ, 762, 72
Trujillo I., Carretero C., Patiri S. G., 2006, ApJ, 640, L111
Varela J., Betancort-Rijo J., Trujillo I., Ricciardelli E., 2012, ApJ, 744, 82
Velliscig M. et al., 2015, MNRAS, 453, 721
Vogelsberger M. et al., 2014, MNRAS, 444, 1518
Wang P., Kang X., 2017, MNRAS, 468, L123
Wang P., Kang X., 2018, MNRAS, 473, 1562
Wang P., Guo Q., Kang X., Libeskind N. I., 2018, ApJ, 866, 138
Welker C., Devriendt J., Dubois Y., Pichon C., Peirani S., 2014, MNRAS, 445, L46
Welker C., Dubois Y., Pichon C., Devriendt J., Chisari N. E., 2018, A&A, 613, A4
White S. D. M., 1984, ApJ, 286, 38
York D. G. et al., 2000, AJ, 120, 1579
Zhang Y., Yang X., Wang H., Wang L., Mo H. J., van den Bosch F. C., 2013, ApJ, 779, 160
Zhang Y., Yang X., Wang H., Wang L., Luo W., Mo H. J., van den Bosch F. C., 2015, ApJ, 798, 17

APPENDIX A: SPIN ALIGNMENT

A1 Galaxy spin flip within walls

Fig. A1 shows redshift and mass evolution of the mean cosine of the angle between the spin of galaxies and the direction vectors of their closest walls $\cos\theta_{w-g}$. A lack of statistics does not allow us to detect a significant evolution of the transition mass with redshift.

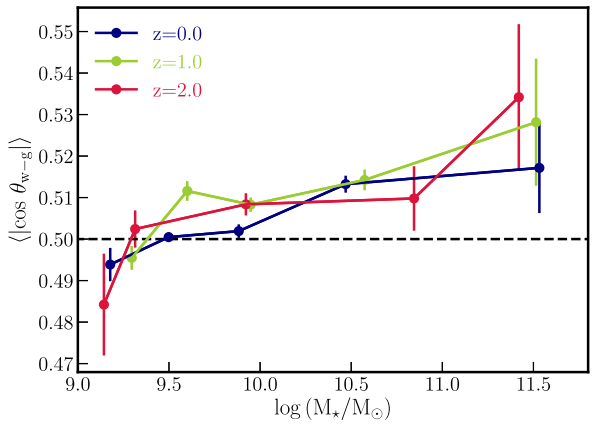

Figure A1. Mean alignment between the spin of galaxies and their closest walls as a function of $M_\star$ at redshifts z =2, 1 and 0, as labelled. The error bars represent the error on the mean among eight subcubes of the simulation. The stellar mass dependent flip of the spin (from parallel to filament at low mass to orthogonal at high mass) is detected.

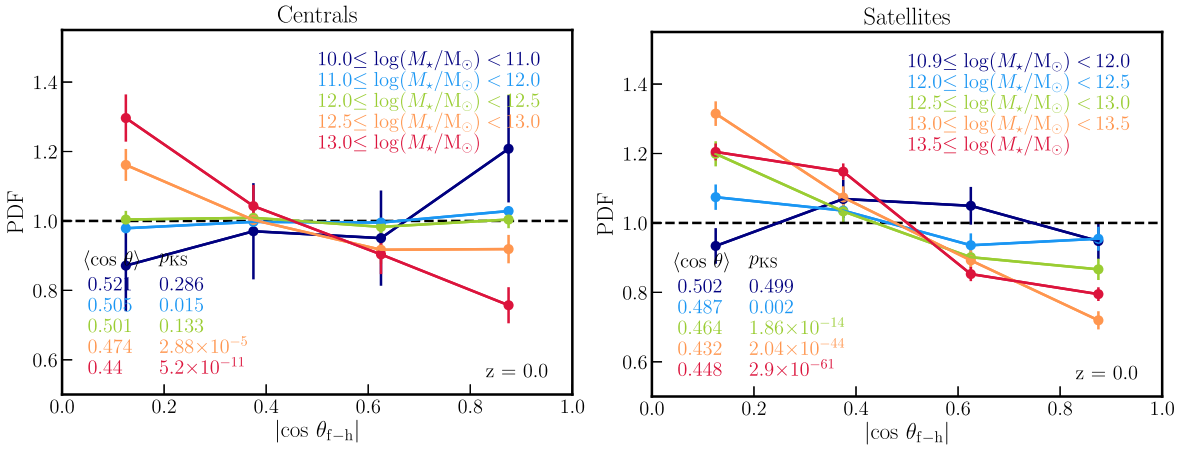

Figure A2. As in Fig. 12, but in different halo mass bins, as labelled. The error bars represent the Poisson noise. Low-mass haloes of centrals tend to align their spin in the direction of closest galaxy's filament. At high mass, all haloes show a clear orthogonal orientation of their spin with respect to filaments. Halos hosting satellites show transition to perpendicular orientation of their spin at lower halo mass compared to haloes of centrals ($\log(M_h/{\rm M}_\odot) \approx 12.0$ compared to $\log(M_h/{\rm M}_\odot) \approx 12.5$).

A2 Galaxies' host spin alignment

Fig. A2 shows the spin alignment of host haloes for centrals and satellites with respect to the filaments obtained from the distribution of galaxies. When splitting by halo mass instead of stellar mass (see Fig. 12), the alignment trend for centrals become more pronounced. For satellites, it is still the case that, except for the lowest mass haloes, they are perpendicularly aligned.

APPENDIX B: KS TEST PROBABILITIES

This Appendix provides the measure of the statistical significance in terms of KS test for all Figures presented in the main text. Tabels B2–B11 contain information about the number of galaxies/haloes, mean cosine of angle between the spin of galaxies/haloes and their host filaments/walls and the KS probability $p_{\rm KS}$ that the sample is drawn from a uniform distribution, for Figs 3–A2.

Table B1. Redshift z, number of haloes $N_{\rm halo}$, average $\cos\theta$ and the KS probability $p_{\rm KS}$ that the sample is drawn from a uniform distribution for Fig. 2.

	z	$M_\star$	$N_{\rm halo}$	$\langle\cos\theta\rangle$	$p_{\rm KS}$
Filaments	0.0	$10.0 \leq \log(M_h/{\rm M}_\odot) < 10.5$	189912	0.508	2.86×10^{-48}
		$10.5 \leq \log(M_h/{\rm M}_\odot) < 11.0$	74431	0.508	1.0×10^{-24}
		$11.0 \leq \log(M_h/{\rm M}_\odot) < 11.5$	26518	0.508	7.5×10^{-7}
		$11.5 \leq \log(M_h/{\rm M}_\odot) < 12.0$	9735	0.505	0.02
		$12.0 \leq \log(M_h/{\rm M}_\odot) < 12.5$	3260	0.496	0.09
		$12.5 \leq \log(M_h/{\rm M}_\odot)$	1705	0.486	0.01
	1.0	$10.0 \leq \log(M_h/{\rm M}_\odot) < 10.5$	228501	0.508	9.8×10^{-62}
		$10.5 \leq \log(M_h/{\rm M}_\odot) < 11.0$	86861	0.507	6.3×10^{-22}
		$11.0 \leq \log(M_h/{\rm M}_\odot) < 11.5$	28335	0.506	3.6×10^{-5}
		$11.5 \leq \log(M_h/{\rm M}_\odot) < 12.0$	10166	0.502	0.32
		$12.0 \leq \log(M_h/{\rm M}_\odot) < 12.5$	3545	0.487	2.7×10^{-5}
		$12.5 \leq \log(M_h/{\rm M}_\odot)$	1255	0.473	6.4×10^{-6}
	2.0	$10.0 \leq \log(M_h/{\rm M}_\odot) < 10.5$	256626	0.508	9.3×10^{-61}
		$10.5 \leq \log(M_h/{\rm M}_\odot) < 11.0$	86148	0.507	3.5×10^{-19}
		$11.0 \leq \log(M_h/{\rm M}_\odot) < 11.5$	26259	0.502	4.5×10^{-3}
		$11.5 \leq \log(M_h/{\rm M}_\odot) < 12.0$	8089	0.496	0.13
		$12.0 \leq \log(M_h/{\rm M}_\odot) < 12.5$	2396	0.477	2.7×10^{-7}
		$12.5 \leq \log(M_h/{\rm M}_\odot)$	575	0.459	5.2×10^{-6}
Walls	0.0	$10.0 \leq \log(M_h/{\rm M}_\odot) < 10.5$	189912	0.491	1.1×10^{-71}
		$10.5 \leq \log(M_h/{\rm M}_\odot) < 11.0$	74431	0.49	1.1×10^{-31}
		$11.0 \leq \log(M_h/{\rm M}_\odot) < 11.5$	26518	0.494	3.1×10^{-8}
		$11.5 \leq \log(M_h/{\rm M}_\odot) < 12.0$	9735	0.502	0.14
		$12.0 \leq \log(M_h/{\rm M}_\odot) < 12.5$	3260	0.508	0.06
		$12.5 \leq \log(M_h/{\rm M}_\odot)$	1705	0.506	0.19
	1.0	$10.0 \leq \log(M_h/{\rm M}_\odot) < 10.5$	228501	0.489	2.6×10^{-124}
		$10.5 \leq \log(M_h/{\rm M}_\odot) < 11.0$	86861	0.489	2.9×10^{-49}

Table B1 *– continued*

	z	$M_\star$	$N_{\rm halo}$	$\langle\cos\theta\rangle$	$p_{\rm KS}$
		$11.0 \leq \log(M_h/{\rm M}_\odot) < 11.5$	28335	0.493	3.8×10^{-11}
		$11.5 \leq \log(M_h/{\rm M}_\odot) < 12.0$	10166	0.5	0.14
		$12.0 \leq \log(M_h/{\rm M}_\odot) < 12.5$	3545	0.508	0.07
		$12.5 \leq \log(M_h/{\rm M}_\odot)$	1255	0.508	0.05
	2.0	$10.0 \leq \log(M_h/{\rm M}_\odot) < 10.5$	256626	0.487	8.4×10^{-194}
		$10.5 \leq \log(M_h/{\rm M}_\odot) < 11.0$	86148	0.489	2.14×10^{-64}
		$11.0 \leq \log(M_h/{\rm M}_\odot) < 11.5$	26259	0.493	8.38×10^{-13}
		$11.5 \leq \log(M_h/{\rm M}_\odot) < 12.0$	8089	0.497	0.02
		$12.0 \leq \log(M_h/{\rm M}_\odot) < 12.5$	2396	0.508	0.03
		$12.5 \leq \log(M_h/{\rm M}_\odot)$	575	0.516	0.02

Table B2. Redshift z, number of galaxies $N_{\rm gal}$, average $\cos\theta$ and the KS probability $p_{\rm KS}$ that the sample is drawn from a uniform distribution for Fig. 3.

	z	$M_\star$	$N_{\rm gal}$	$\langle\cos\theta\rangle$	$p_{\rm KS}$
Filaments	0.0	$9.0 \leq \log(M_\star/{\rm M}_\odot) < 9.5$	8624	0.507	3.91×10^{-4}
		$9.5 \leq \log(M_\star/{\rm M}_\odot) < 10.0$	13498	0.501	0.918
		$10.0 \leq \log(M_\star/{\rm M}_\odot) < 10.5$	6836	0.499	0.026
		$10.5 \leq \log(M_\star/{\rm M}_\odot) < 11.0$	2584	0.484	1.66×10^{-4}
		$11.0 \leq \log(M_\star/{\rm M}_\odot)$	735	0.473	4.48×10^{-6}
	1.0	$9.0 \leq \log(M_\star/{\rm M}_\odot) < 9.5$	5623	0.505	8.0×10^{-3}
		$9.5 \leq \log(M_\star/{\rm M}_\odot) < 10.0$	5656	0.501	0.405
		$10.0 \leq \log(M_\star/{\rm M}_\odot) < 10.5$	4571	0.497	0.075
		$10.5 \leq \log(M_\star/{\rm M}_\odot) < 11.0$	2305	0.489	2.0×10^{-3}
		$11.0 \leq \log(M_\star/{\rm M}_\odot)$	626	0.469	3.16×10^{-5}
	2.0	$9.0 \leq \log(M_\star/{\rm M}_\odot) < 9.5$	4123	0.506	0.011
		$9.5 \leq \log(M_\star/{\rm M}_\odot) < 10.0$	2945	0.501	0.51
		$10.0 \leq \log(M_\star/{\rm M}_\odot) < 10.5$	1594	0.496	0.16
		$10.5 \leq \log(M_\star/{\rm M}_\odot) < 11.0$	835	0.497	0.463
		$11.0 \leq \log(M_\star/{\rm M}_\odot)$	341	0.47	2.37×10^{-4}
Walls	0.0	$9.0 \leq \log(M_\star/{\rm M}_\odot) < 9.5$	8624	0.497	0.137
		$9.5 \leq \log(M_\star/{\rm M}_\odot) < 10.0$	13498	0.502	0.309
		$10.0 \leq \log(M_\star/{\rm M}_\odot) < 10.5$	6836	0.507	2.57×10^{-5}
		$10.5 \leq \log(M_\star/{\rm M}_\odot) < 11.0$	2584	0.519	5.57×10^{-9}
		$11.0 \leq \log(M_\star/{\rm M}_\odot)$	735	0.523	2.81×10^{-4}
	1.0	$9.0 \leq \log(M_\star/{\rm M}_\odot) < 9.5$	5623	0.495	0.021
		$9.5 \leq \log(M_\star/{\rm M}_\odot) < 10.0$	5656	0.509	1.68×10^{-4}
		$10.0 \leq \log(M_\star/{\rm M}_\odot) < 10.5$	4571	0.511	2.3×10^{-5}
		$10.5 \leq \log(M_\star/{\rm M}_\odot) < 11.0$	2305	0.513	1.0×10^{-3}
		$11.0 \leq \log(M_\star/{\rm M}_\odot)$	626	0.534	1.13×10^{-7}
	2.0	$9.0 \leq \log(M_\star/{\rm M}_\odot) < 9.5$	4123	0.5	0.754
		$9.5 \leq \log(M_\star/{\rm M}_\odot) < 10.0$	2945	0.507	0.084
		$10.0 \leq \log(M_\star/{\rm M}_\odot) < 10.5$	1594	0.513	2.4×10^{-4}
		$10.5 \leq \log(M_\star/{\rm M}_\odot) < 11.0$	835	0.504	0.152
		$11.0 \leq \log(M_\star/{\rm M}_\odot)$	341	0.527	3.42×10^{-4}

Table B3. Number of galaxies, average $\cos\theta$ and the KS probability $p_{\rm KS}$ that the sample is drawn from a uniform distribution for Fig. 5.

	$M_\star$ range	$N_{\rm gal}$	$\langle\cos\theta\rangle$	$p_{\rm KS}$
Low v/σ	$9.0 \leq \log(M_\star/{\rm M}_\odot) < 9.5$	5946	0.505	0.032
	$9.5 \leq \log(M_\star/{\rm M}_\odot) < 10.0$	10967	0.501	0.688
	$10.0 \leq \log(M_\star/{\rm M}_\odot) < 10.5$	4514	0.501	0.078
	$10.5 \leq \log(M_\star/{\rm M}_\odot) < 11.0$	1119	0.479	2.3×10^{-5}
	$11.0 \leq \log(M_\star/{\rm M}_\odot)$	385	0.472	9.6×10^{-3}
High v/σ	$9.0 \leq \log(M_\star/{\rm M}_\odot) < 9.5$	2335	0.512	1.9×10^{-3}
	$9.5 \leq \log(M_\star/{\rm M}_\odot) < 10.0$	2518	0.499	0.917
	$10.0 \leq \log(M_\star/{\rm M}_\odot) < 10.5$	2267	0.493	2.7×10^{-3}
	$10.5 \leq \log(M_\star/{\rm M}_\odot) < 11.0$	1427	0.488	0.014
	$11.0 \leq \log(M_\star/{\rm M}_\odot)$	320	0.486	0.013

Table B4. Number of galaxies, average $\cos\theta$ and the KS probability $p_{\rm KS}$ that the sample is drawn from a uniform distribution for Fig. 6.

	$M_\star$ range	$N_{\rm gal}$	$\langle\cos\theta\rangle$	$p_{\rm KS}$
Low sSFR	$9.0 \leq \log(M_\star/{\rm M}_\odot) < 9.5$	1407	0.509	0.021
	$9.5 \leq \log(M_\star/{\rm M}_\odot) < 10.0$	2696	0.503	0.749
	$10.0 \leq \log(M_\star/{\rm M}_\odot) < 10.5$	4172	0.499	0.192
	$10.5 \leq \log(M_\star/{\rm M}_\odot) < 11.0$	1789	0.482	4.3×10^{-5}
	$11.0 \leq \log(M_\star/{\rm M}_\odot)$	606	0.475	1.6×10^{-4}
High sSFR	$9.0 \leq \log(M_\star/{\rm M}_\odot) < 9.5$	6876	0.507	2.9×10^{-3}
	$9.5 \leq \log(M_\star/{\rm M}_\odot) < 10.0$	10802	0.5	0.916
	$10.0 \leq \log(M_\star/{\rm M}_\odot) < 10.5$	2664	0.498	0.078
	$10.5 \leq \log(M_\star/{\rm M}_\odot) < 11.0$	795	0.489	0.129
	$11.0 \leq \log(M_\star/{\rm M}_\odot)$	129	0.465	0.014

Table B5. Number of galaxies, average $\cos\theta$ and the KS probability $p_{\rm KS}$ that the sample is drawn from a uniform distribution for Fig. 7.

	$M_\star$ range	$N_{\rm gal}$	$\langle\cos\theta\rangle$	$p_{\rm KS}$
Low HI mass	$9.0 \leq \log(M_\star/{\rm M}_\odot) < 9.5$	2237	0.502	0.542
	$9.5 \leq \log(M_\star/{\rm M}_\odot) < 10.0$	5866	0.497	0.397
	$10.0 \leq \log(M_\star/{\rm M}_\odot) < 10.5$	3001	0.498	0.061
	$10.5 \leq \log(M_\star/{\rm M}_\odot) < 11.0$	816	0.47	7.3×10^{-6}
	$11.0 \leq \log(M_\star/{\rm M}_\odot)$	192	0.464	2.2×10^{-4}
High HI mass	$9.0 \leq \log(M_\star/{\rm M}_\odot) < 9.5$	4828	0.508	6.6×10^{-3}
	$9.5 \leq \log(M_\star/{\rm M}_\odot) < 10.0$	6243	0.502	0.707
	$10.0 \leq \log(M_\star/{\rm M}_\odot) < 10.5$	3103	0.498	0.124
	$10.5 \leq \log(M_\star/{\rm M}_\odot) < 11.0$	1411	0.491	0.15
	$11.0 \leq \log(M_\star/{\rm M}_\odot)$	488	0.476	3.2×10^{-3}

Table B6. Number of galaxies, average $\cos\theta$ and the KS probability $p_{\rm KS}$ that the sample is drawn from a uniform distribution for Fig. 9.

	$M_\star$ range	$N_{\rm gal}$	$\langle\cos\theta\rangle$	$p_{\rm KS}$
Low M_h	$9.0 \leq \log(M_\star/{\rm M}_\odot) < 9.5$	5513	0.506	0.025
	$9.5 \leq \log(M_\star/{\rm M}_\odot) < 10.0$	9023	0.5	0.747
	$10.0 \leq \log(M_\star/{\rm M}_\odot) < 10.5$	1310	0.504	0.122
	$10.5 \leq \log(M_\star/{\rm M}_\odot) < 11.0$	11	0.524	0.615
High M_h	$9.0 \leq \log(M_\star/{\rm M}_\odot) < 9.5$	2770	0.509	0.002
	$9.5 \leq \log(M_\star/{\rm M}_\odot) < 10.0$	4475	0.501	0.891
	$10.0 \leq \log(M_\star/{\rm M}_\odot) < 10.5$	5526	0.497	0.019
	$10.5 \leq \log(M_\star/{\rm M}_\odot) < 11.0$	2573	0.484	1.4×10^{-4}
	$11.0 \leq \log(M_\star/{\rm M}_\odot)$	735	0.473	4.5×10^{-6}

Table B7. Number of galaxies, average $\cos\theta$ and the KS probability $p_{\rm KS}$ that the sample is drawn from a uniform distribution for Fig. 10.

	$M_\star$ range	$N_{\rm gal}$	$\langle\cos\theta\rangle$	$p_{\rm KS}$
Centrals	$9.0 \leq \log(M_\star/{\rm M}_\odot) < 9.5$	5251	0.507	6.5×10^{-3}
	$9.5 \leq \log(M_\star/{\rm M}_\odot) < 10.0$	9443	0.501	0.82
	$10.0 \leq \log(M_\star/{\rm M}_\odot) < 10.5$	4535	0.496	7.3×10^{-4}
	$10.5 \leq \log(M_\star/{\rm M}_\odot) < 11.0$	1775	0.48	1.3×10^{-5}
	$11.0 \leq \log(M_\star/{\rm M}_\odot)$	579	0.472	6.7×10^{-5}
Satellites	$9.0 \leq \log(M_\star/{\rm M}_\odot) < 9.5$	3032	0.506	0.032
	$9.5 \leq \log(M_\star/{\rm M}_\odot) < 10.0$	4055	0.501	0.891
	$10.0 \leq \log(M_\star/{\rm M}_\odot) < 10.5$	2301	0.503	0.104
	$10.5 \leq \log(M_\star/{\rm M}_\odot) < 11.0$	809	0.493	0.219
	$11.0 \leq \log(M_\star/{\rm M}_\odot)$	156	0.478	0.01

Table B8. Number of galaxies, average $\cos\theta$ and the KS probability $p_{\rm KS}$ that the sample is drawn from a uniform distribution for Fig. 13.

	$M_\star$ range	$N_{\rm gal}$	$\langle\cos\theta\rangle$	$p_{\rm KS}$
Low ρ_f	$9.0 \leq \log(M_\star/{\rm M}_\odot) < 9.5$	2237	0.506	0.248
	$9.5 \leq \log(M_\star/{\rm M}_\odot) < 10.0$	3884	0.504	0.175
	$10.0 \leq \log(M_\star/{\rm M}_\odot) < 10.5$	1483	0.497	0.042
	$10.5 \leq \log(M_\star/{\rm M}_\odot) < 11.0$	358	0.483	0.21
	$11.0 \leq \log(M_\star/{\rm M}_\odot)$	42	0.44	0.031
High ρ_f	$9.0 \leq \log(M_\star/{\rm M}_\odot) < 9.5$	2057	0.51	1.2×10^{-3}
	$9.5 \leq \log(M_\star/{\rm M}_\odot) < 10.0$	2739	0.497	0.118
	$10.0 \leq \log(M_\star/{\rm M}_\odot) < 10.5$	1799	0.499	0.517
	$10.5 \leq \log(M_\star/{\rm M}_\odot) < 11.0$	925	0.495	0.464
	$11.0 \leq \log(M_\star/{\rm M}_\odot)$	466	0.474	7.6×10^{-4}

Table B9. Number of galaxies, average $\cos\theta$ and the KS probability $p_{\rm KS}$ that the sample is drawn from a uniform distribution for Fig. 11.

	$M_\star$	$N_{\rm gal}$	$\langle\cos\theta\rangle$	$p_{\rm KS}$
Centrals	$9.0 \leq \log(M_\star/{\rm M}_\odot) < 9.5$	5250	0.577	2.5×10^{-72}
	$9.5 \leq \log(M_\star/{\rm M}_\odot) < 10.0$	9433	0.58	2.0×10^{-129}
	$10.0 \leq \log(M_\star/{\rm M}_\odot) < 10.5$	4494	0.599	2.8×10^{-90}
	$10.5 \leq \log(M_\star/{\rm M}_\odot) < 11.0$	1711	0.583	0.0
	$11.0 \leq \log(M_\star/{\rm M}_\odot)$	587	0.531	9.3×10^{-3}
Satellites	$9.0 \leq \log(M_\star/{\rm M}_\odot) < 9.5$	3031	0.497	0.484
	$9.5 \leq \log(M_\star/{\rm M}_\odot) < 10.0$	4051	0.508	0.027
	$10.0 \leq \log(M_\star/{\rm M}_\odot) < 10.5$	2287	0.499	0.398
	$10.5 \leq \log(M_\star/{\rm M}_\odot) < 11.0$	801	0.49	0.35
	$11.0 \leq \log(M_\star/{\rm M}_\odot)$	152	0.503	0.991

Table B10. Number of galaxies, average $\cos\theta$ and the KS probability $p_{\rm KS}$ that the sample is drawn from a uniform distribution for Fig. 12.

	$M_\star$	$N_{\rm gal}$	$\langle\cos\theta\rangle$	$p_{\rm KS}$
Centrals	$9.0 \leq \log(M_\star/{\rm M}_\odot) < 9.5$	5250	0.504	0.022
	$9.5 \leq \log(M_\star/{\rm M}_\odot) < 10.0$	9433	0.504	0.076
	$10.0 \leq \log(M_\star/{\rm M}_\odot) < 10.5$	4494	0.501	0.432
	$10.5 \leq \log(M_\star/{\rm M}_\odot) < 11.0$	1711	0.488	7.6×10^{-3}
	$11.0 \leq \log(M_\star/{\rm M}_\odot)$	587	0.453	4.0×10^{-6}
Satellites	$9.0 \leq \log(M_\star/{\rm M}_\odot) < 9.5$	3031	0.497	0.484
	$9.5 \leq \log(M_\star/{\rm M}_\odot) < 10.0$	4051	0.508	0.027
	$10.0 \leq \log(M_\star/{\rm M}_\odot) < 10.5$	2287	0.499	0.398
	$10.5 \leq \log(M_\star/{\rm M}_\odot) < 11.0$	801	0.49	0.350
	$11.0 \leq \log(M_\star/{\rm M}_\odot)$	152	0.503	0.991

Table B11. Number of galaxies, average $\cos\theta$ and the KS probability $p_{\rm KS}$ that the sample is drawn from a uniform distribution for Fig. A2.

	$M_\star$	$N_{\rm gal}$	$\langle\cos\theta\rangle$	$p_{\rm KS}$
Centrals	$10.0 \leq \log(M_h/{\rm M}_\odot) < 11.0$	101	0.521	0.286
	$11.0 \leq \log(M_h/{\rm M}_\odot) < 12.0$	16500	0.505	0.015
	$12.0 \leq \log(M_h/{\rm M}_\odot) < 12.5$	3217	0.501	0.133
	$12.5 \leq \log(M_h/{\rm M}_\odot) < 13.0$	1097	0.474	2.9×10^{-5}
	$13.0 \leq \log(M_h/{\rm M}_\odot)$	560	0.44	5.2×10^{-11}
Satellites	$10.9 \leq \log(M_h/{\rm M}_\odot) < 12.0$	709	0.502	0.49
	$12.0 \leq \log(M_h/{\rm M}_\odot) < 12.5$	1603	0.487	1.9×10^{-3}
	$12.5 \leq \log(M_h/{\rm M}_\odot) < 13.0$	1833	0.464	1.8×10^{-14}
	$13.0 \leq \log(M_h/{\rm M}_\odot) < 13.5$	2096	0.432	2.0×10^{-44}
	$13.5 \leq \log(M_h/{\rm M}_\odot)$	4081	0.448	2.9×10^{-61}

This paper has been typeset from a TEX/LATEX file prepared by the author.